



Theses and Dissertations

2020-08-04

Breaking the Organic Mold: Introducing Copper into the Influenza A Arena with Neutral and Divalent Complexes

Jonathan D. Lynch
Brigham Young University

Follow this and additional works at: <https://scholarsarchive.byu.edu/etd>

 Part of the [Physical Sciences and Mathematics Commons](#)

BYU ScholarsArchive Citation

Lynch, Jonathan D., "Breaking the Organic Mold: Introducing Copper into the Influenza A Arena with Neutral and Divalent Complexes" (2020). *Theses and Dissertations*. 8677.
<https://scholarsarchive.byu.edu/etd/8677>

This Thesis is brought to you for free and open access by BYU ScholarsArchive. It has been accepted for inclusion in Theses and Dissertations by an authorized administrator of BYU ScholarsArchive. For more information, please contact ellen_amatangelo@byu.edu.

Breaking the Organic Mold: Introducing Copper into the
Influenza A Arena with Neutral and
Divalent Complexes

Jonathan D. Lynch

A thesis submitted to the faculty of
Brigham Young University
in partial fulfillment of the requirements for the degree of
Master of Science

Roger G. Harrison, Chair
David D. Busath
Richard K. Watt

Department of Chemistry and Biochemistry
Brigham Young University

Copyright © 2020 Jonathan D. Lynch

All Rights Reserved

ABSTRACT

Breaking the Organic Mold: Introducing Copper into the Influenza A M2 Arena with Neutral and Divalent Complexes

Jonathan D. Lynch

Department of Chemistry and Biochemistry, BYU
Master of Science

Influenza A (IVA) continues to pose a growing global threat even as current medications are becoming less effective. One of the main avenues of research into new anti-IVA drugs is its homotetrameric Matrix 2 proton channel (M2A), without which the virus would be unable to release its viral RNA into the host cell. The drug amantadine used to bind and block M2A until near-ubiquitous resistance formed as an M2A-S31N mutation, starting around 1995 and proceeding to 2005 when amantadine was disallowed for use as an anti-IVA drug. The standard organic structure currently being used for M2A inhibitor research comprises an adamantyl foot group, a heterocyclic aryl body group, and a cyclic head group. A sample set of compounds with this standard structure was compared and reviewed, focusing on positive and negative moieties and modifications. Modifications on the foot group were all more or less detrimental, body groups with two heteroatoms were advantageous, and larger head groups appeared better. Four other scaffolds known to literature were proposed for further study due to beneficial aspects of each.

Where most anti-M2A research deals exclusively with organic compounds, metals and their potential in drugs have been almost entirely ignored due to the increased toxicity they bring. Free copper was found in past research to be the only first-row transition metal to show significant M2A-inhibitory activity, proposed to do so by binding the H37 cluster that acts as a pH-dependent control switch for the channel. Six overall-neutral copper complexes were synthesized as a combination of amantadine, cyclooctylamine, and null scaffolds with two of either acetate or acetamide arms as chelators. The complexes were found to block both M2A-WT and M2A-S31N. Along with CuCl_2 , though, they had little to no effect on M2A-H37A, providing confirming evidence that the copper binds at the H37 tetrad. Only one complex, $\text{Cu}(\text{cyclooctylamineiminodiacetate})$, outperformed CuCl_2 in channel block studies and efficacy against two IVA strains, but all of the complexes were found to have lower cytotoxicity. Because M2-H37 is highly conserved, these complexes show promise for further testing against all strains of influenza A.

Five net-divalent copper complexes were then synthesized with multiple aza or amine groups as chelators. The complexes failed to show any significant activity against M2A, however, which was thought to be due to size or polarity rejection or electromagnetic repulsion. One of the ligands, though, an adamantyl derivative of a tetraaza macrocycle, was a novel compound, and its copper complex, along with two others, were unknown to the CCDC database. The three complexes were characterized by X-ray diffraction and discussed.

Keywords: medicinal metals, tridentate or tetradentate chelation, proton transport, cyclen crystal

ACKNOWLEDGEMENTS

I would like to thank Dr. Roger Harrison for being the best, kindest, most patient mentor and advisor I could ever have asked for. It was divine providence that led me to your group, and I couldn't be more grateful. I also want to express deep appreciation for my committee members final and past, Drs. David Busath, Richard Watt, Kara Stowers, and David Michaelis, who pushed me when I needed it most and revolutionized the way I think about my role as a scientist.

Thank you to my children, Nikolai and Taylin, for your patience and love during the writing of this thesis. You've shown understanding and dedication far beyond your short years.

And, of course, my biggest thanks go to my lovely wife, Meagan. You've stood by me and sacrificed for me when I was sure I wasn't worth it. I'm so glad we've been promised eternity together, because anything less would feel too short. I look forward to spending every day of it with you.

TABLE OF CONTENTS

TITLE PAGE	i
ABSTRACT	ii
ACKNOWLEDGEMENTS	iii
TABLE OF CONTENTS.....	iv
LIST OF TABLES.....	viii
LIST OF FIGURES	ix
CHAPTER 1: Optimization of Organic Influenza A M2-S31N Channel Inhibitors: A Review of Commonalities and Differences.....	1
Abstract	1
Introduction.....	1
General selection criteria and synthesis techniques.....	7
Determination of antiviral properties.....	8
Comparison of chosen compounds	9
Comparison of head groups	13
Comparison of body groups.....	15
Comparison of foot groups	16
Comparison of non-amantadine structures	17
Efficacy, cytotoxicity, therapeutic index, and liver stability	18
Conclusions.....	19

References.....	21
CHAPTER 2: Introducing Copper into the Arena of Influenza A M2 Inhibitors Using Net	
Neutral Complexes with Acid and Amide Chelation	23
Abstract	23
1. Introduction.....	23
2. Materials and methods	27
2.1. Instruments and materials	27
2.2 Compound and complex synthesis.....	28
2.2.1. Synthesis of N-(1-adamantyl)-iminodiacetic acid (1).....	28
2.2.2. Synthesis of Copper N-(1-adamantyl)-iminodiacetic acid (2).....	28
2.2.3. Synthesis of Cyclooctyliminodiacetic acid (3)	29
2.2.4. Synthesis of Copper cyclooctyliminodiacetic acid (4)	29
2.2.5. Synthesis of Amt-iminodiacetamide (5)	30
2.2.6. Synthesis of Cu(Amt-iminodiacetamide) (6).....	30
2.2.7. Synthesis of Cyclooctylimidodiacetamide (7).....	31
2.2.8. Synthesis of Copper cyclooctylimidodiacetamide (8)	32
2.2.9. Synthesis of Copper iminodiacetic acid (9)	32
2.2.10. Synthesis of Copper iminodiacetamide (10).....	33
2.3. Stability Studies	33
2.4. Electrophysiology	34

2.5. Cell culture.....	34
2.6. Cytotoxicity assay	34
2.7. Viral infection assay	35
3. Results and discussion	36
3.1. Compound and complex synthesis and structure.....	36
3.2. Stability studies.....	38
3.3. ¹ H-NMR characterization	40
3.4. Antiviral properties	40
4. Conclusions.....	44
Acknowledgements.....	45
References.....	45
CHAPTER 3: Crystal Structures and Influenza A Inhibition of Divalent Polyamine Copper	
Complexes	48
Abstract.....	48
1. Introduction.....	48
2. Experimental	52
2.1. Synthesis	52
2.1.1. General considerations.....	52
2.1.2. Synthesis of Cu(Cyclen)Cl ₂ (1)	53
2.1.3. Synthesis of Cu(Cyclen)(ClO ₄) ₂ (2).....	53

2.1.4. Synthesis of N-((adamant-1-yl)methyl)-cyclen (3L).....	53
2.1.5. Synthesis of [Cu(N-((adamant-1-yl)methyl)-cyclen)]SO ₄ (3)	54
2.1.6. Synthesis of TACN (4L).....	54
2.1.7. Synthesis of [Cu(TACN)]SO ₄ (4).....	54
2.1.8. Synthesis of N,N'-bis(2-pyridylmethyl)amantadine (5L)	55
2.1.9. Synthesis of [Cu(N,N'-bis(2-pyridylmethyl)amantadine)]SO ₄ (5)....	55
2.2. Refinement	55
3. Results and Discussion	56
3.1. Synthesis of 3L and 3	56
3.2. Crystal structures	60
3.3 Viral studies	67
4. Conclusions.....	69
Acknowledgements.....	70
References.....	70

LIST OF TABLES

Table 1.1. Compounds and derivatives for comparison of M2A S31N block, efficacy against IVA H1N1 M2A S31N, cytotoxicity, and liver stability.	10
Table 2.1. Cytotoxicity and efficacy data for CuCl ₂ , 2 , 4 , 6 , 8 , 9 , and 10	41
Table 2.2. M2 block of CuCl ₂ , Amt, 2 , 3 , 4 , 6 , 8 , 9 , and 10	42
Table 3.1. Crystallography data for 1 , 2 , and 3	61
Table 3.2. Selected bond lengths and distances (Å).	63

LIST OF FIGURES

Figure 1.1. Infection cycle of IVA in a host cell.	3
Figure 1.2. Acid activation mechanism of the M2A channel.	3
Figure 1.3. Amantadine binding position in M2A.	4
Figure 1.4. Design indicators and customizability of M2A-S31N inhibitors.	5
Figure 1.5. Parent compounds selected for comparison.	6
Figure 1.6. Example synthetic route to potential candidates for M2A-S31N inhibition.	8
Figure 2.1. Copper complexes with the functional groups iminodiacetate or iminodiacetamide extended via the amine to either AMT or CO.	26
Figure 2.2. Synthetic procedures for compounds 1-8	37
Figure 2.3. Crystal structure (side and face views) of 2	37
Figure 2.4. UV–Vis spectra of 100 μ M solutions of 2 , 4 , 6 , and 8 in water.	39
Figure 2.5. UV-Vis spectra of 100 μ M solutions of 2 , 4 , 6 , and 8 in SEM.	39
Figure 2.6. UV-Vis spectra of 100 μ M solutions of 2 , 4 , 6 , and 8 in Barth's.	39
Figure 2.7. ^1H -NMR (300 MHz) of 2 with an acetonitrile standard before acidification in DMSO- d_6	40
Figure 2.8. ^1H -NMR (300 MHz) of 2 with an acetonitrile standard after acidification with trifluoroacetic acid in DMSO- d_6	41
Figure 2.9. TEVC traces in Barth's solution of CuCl_2 , 4 , and 3	43
Figure 3.1. Structures of neutral and divalent copper complexes.	50
Figure 3.2: ^1H -NMR (500 MHz) of 3L in CDCl_3 before addition of methanol- d_4	57
Figure 3.3: ^1H -NMR (500 MHz) of 3L in CDCl_3 after addition of 2 drops of methanol- d_4	57
Figure 3.4: ^1H -NMR (500 MHz) of 3 in DMSO- d_6 before adding deuterium chloride.	58

Figure 3.5: ^1H -NMR (500 MHz) of 3 in DMSO- d_6 after addition of deuterium chloride.....	58
Figure 3.6. Mass spectrum of 3L	59
Figure 3.7. Mass spectrum of 3	59
Figure 3.8. Hydrogen bonding in the crystal lattice of 1	62
Figure 3.9. Crystal structures of 1 , 2 , and 3	63
Figure 3.10. Crystal structures of two conformers of 1	64
Figure 3.11. Hydrogen bonding in the crystal lattice of 3	65
Figure 3.12. Crystal packing structure of 3	66
Figure 3.13. Crystal packing structure of 1	68
Figure 3.14. Crystal packing structure of 2	68

CHAPTER 1

Optimization of Organic Influenza A M2-S31N Channel Inhibitors:

A Review of Commonalities and Differences

Abstract

Research on inhibiting influenza A Matrix 2 protein (M2A) spans a number of methods with overlap among research groups; focus on methods that have shown positive results would help in drug development of new M2A inhibitors. A comparison of a select sample set of compounds from the literature is given, focusing on finding beneficial and detrimental modifications to the standard structure currently being used for inhibitors, comprising an amantadyl foot group, a heterocyclic aryl body group, and a cyclic head group. The unmodified amantadyl moiety was found to be the best foot group, though alcohol addition provided mixed results. The best body groups were found to be those with two substituted carbons in the ring, namely, for the sample set in this study, 2-azafuran and pyrazine. The best head groups were found to be larger ring systems, either from addition of side groups or larger ring sizes; sizes up to 8-membered rings were compared with increasing channel block. Aromaticity of the head group seemed to make little to no difference. Derivatives of amantadine, rimantadine, spiropiperidine, and cyclooctylamine are also proposed as alternative foot groups with different constraints and customizability than amantadine.

Introduction

In the western hemisphere alone, disease associated with seasonal influenza virus A (IVA) causes approximately 85,000 human deaths annually.¹ While most viruses exhibit either high transmittance or high mortality, modern mutations in IVA have pointed inexorably toward the evolution of a virus with both characteristics, making a disastrous pandemic in the future

inevitable.² Indeed, the World Health Organization has called the looming pandemic an “evolving threat,” emphasizing that any local outbreak of such a mutant IVA strain could rapidly become a global problem.³ In light of this threat, governments across the globe have, in recent years, prioritized IVA research in an attempt to minimize the loss of life from the predicted pandemic.⁴

Much of this anti-IVA research is geared toward developing therapeutics to treat influenza A patients more quickly and effectively than current methods, as opposed to those that act in a prophylactic capacity. Those treatments would be expected to help infected persons overcome the illness faster while decreasing the mortality rate associated with influenza infections by helping terminal infection cases end without loss of human life. Additionally, in the case of an IVA pandemic, in which prophylactics show little to no effectiveness, these products would give humanity an edge over the virus. As punctuated by the current extent of the COVID-19 pandemic, such an edge could potentially save millions of jeopardized lives against the onslaught of a dramatically mutated virus strain.

Research on combating IVA spans a variety of targets. This review focuses on the essential M2 proton channel (M2A), a critical component of the virus’s infection cycle. M2A acidification inside endocytic organelles initiates the release of viral genetic material into the host cell (Figure 1.1), making inhibition of M2A an effective means to prevent IVA from replicating and the infection from progressing.^{5,6} Because the purpose of M2A inhibition is to block proton flow through the channel, understanding the mechanism of proton transfer is important. At high pH, the His37 tetrad has, at most, 2 of the residue side chains protonated, and the channel remains in the closed position (Figure 1.2, left). The closed conformation is further stabilized by a hydrogen-bonding network formed among the Trp41 residues.⁷ As the pH drops to be acidic, a

third residue becomes protonated, and the channel activates to the open position (Figure 1.2, right).⁸

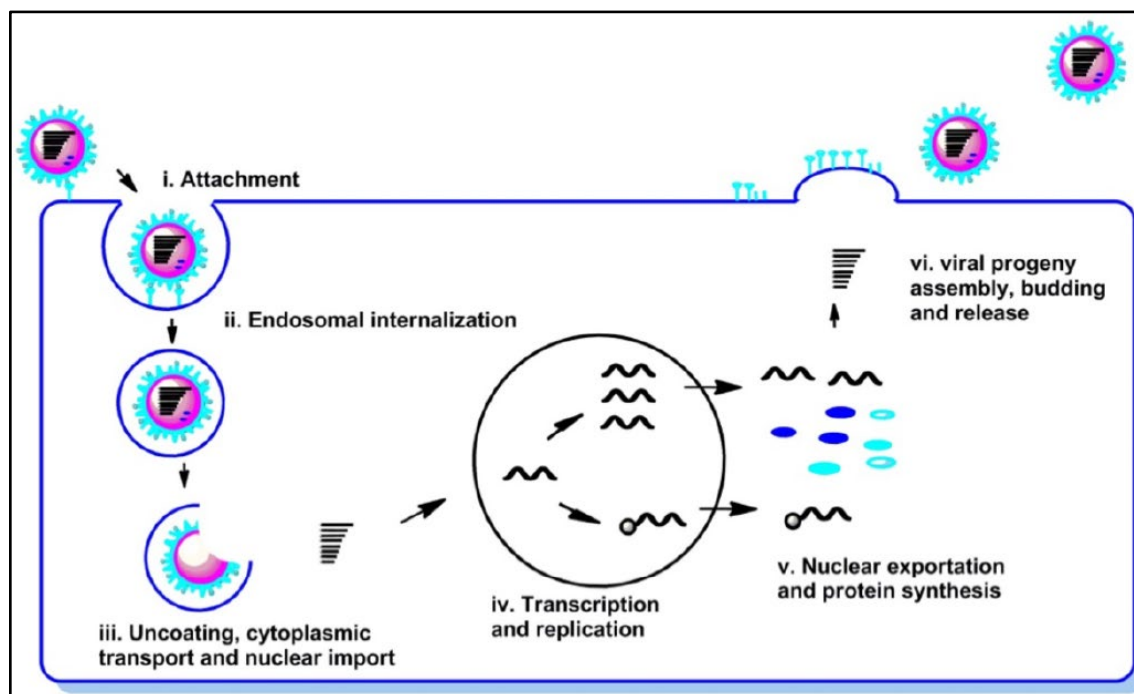


Figure 1.1. Infection cycle of IVA in a host cell.

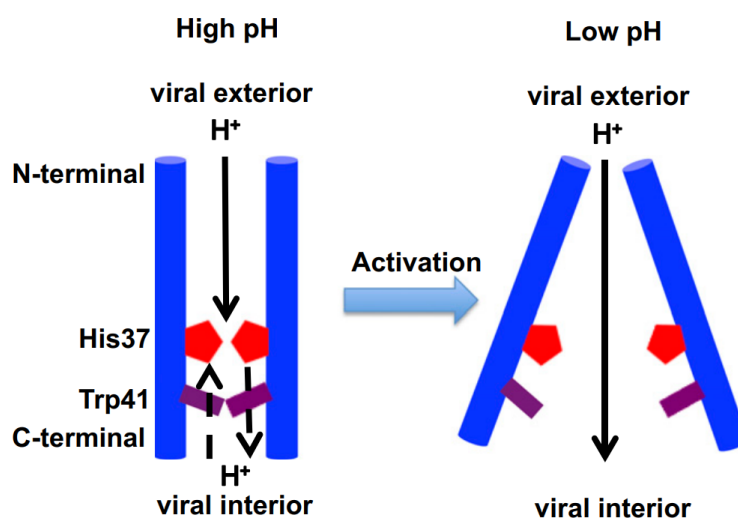


Figure 1.2. Acid activation mechanism of the M2A channel.

Further study of M2A through NMR and X-ray crystallography has failed to conclusively determine the mechanism of activation.⁹ However, the leading model at the time of this writing suggests that electrostatic repulsion among the 3-4 positively-charged His37 residues forces the

C-terminal side of the channel to spread open.¹⁰ According to the Grotthuss mechanism, proton transfer then proceeds through a lattice of water molecules without changing the protonation state at the His37 cluster.¹¹ The primary goal in inhibiting M2A, then, must be to prevent access of hydronium to the channel interior and particularly to the His37 cluster.

M2A is a known target for the adamantane-containing compound amantadine (1-adamantylamine, Amt), in which the amine binds the S31 site and the homotetracycle is stabilized by hydrophobic interactions with the V27 tetrad. In this position, the adamantane disrupts water flow transfer through the channel (Figure 1.3, left).^{12,13} By 2005, however, Amt resistance became nearly universal across all strains via an S31N mutation of the channel that flipped the Amt to an up-facing orientation, replacing the stabilizing influence of valine with the less available glycine and allowing water to flow, barely inhibited, around the compound (Figure 1.3, right).¹⁴ This development led the CDC to recommend against prescribing adamantanes as anti-IVA agents.¹⁵

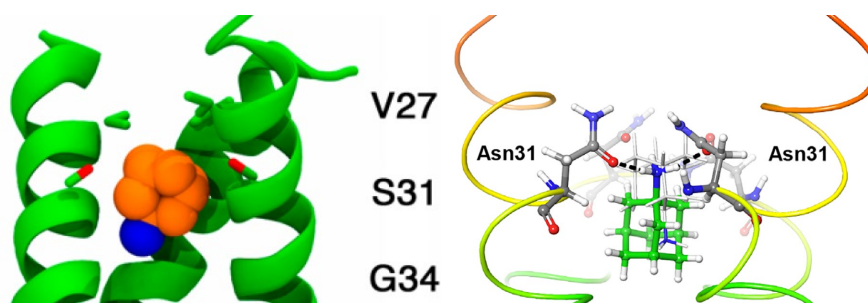


Figure 1.3. Amantadine binding position in M2A. The wildtype IVA M2A channel is shown as green ribbons (the front being removed for clarity) and the amantadine carbons as orange space-filling spheres (left), and the M2A-S31N mutant is shown with the channel depicted by thin tubes (the front and back being removed for clarity) and the amantadine carbons by a green ball-and-stick model (right).

Since then, several groups have been performing research toward developing novel M2A-inhibitory drugs, focusing on amantadines, rimantadines, and other adamantyl derivatives, as well as a number of other moieties. Predictably, the numerous trial compounds tested in that time

have varied to many degrees in their capacity to block M2A, with some succeeding quite well while many showed little to no activity. A better understanding of the similarities among successful compounds and the differences between successful and unsuccessful compounds, both of which are explored herein, could serve to narrow compound-search parameters in future M2A-inhibition research.

Amt derivatives most often form from N-substitutions, though sometimes substituents, especially hydroxyl or methyl groups, are added to the ring itself.¹⁶ Observation of a pharmacophore for inhibitors (Figure 1.4, A) within the M2A-S31N mutant reveals that the bulky ring system is able to find a relatively stable pocket within the hydrophobic G34 cavity, while the amine forms hydrogen bonds with the N31 carbonyl cluster.¹⁷ The foot group can be altered in a number of ways to better suit the conditions of the M2A system (Figure 1.4, B).¹⁸ The aryl body group is further capable of acting as a hydrogen bond acceptor from the N31 amide cluster, either through the π orbitals or through O, N, or S substitution for a ring carbon.¹⁹ Finally, the aliphatic or aryl head group is able to form stabilizing hydrophobic interactions with the V27 cluster. It should be noted that while this general design has been confirmed through

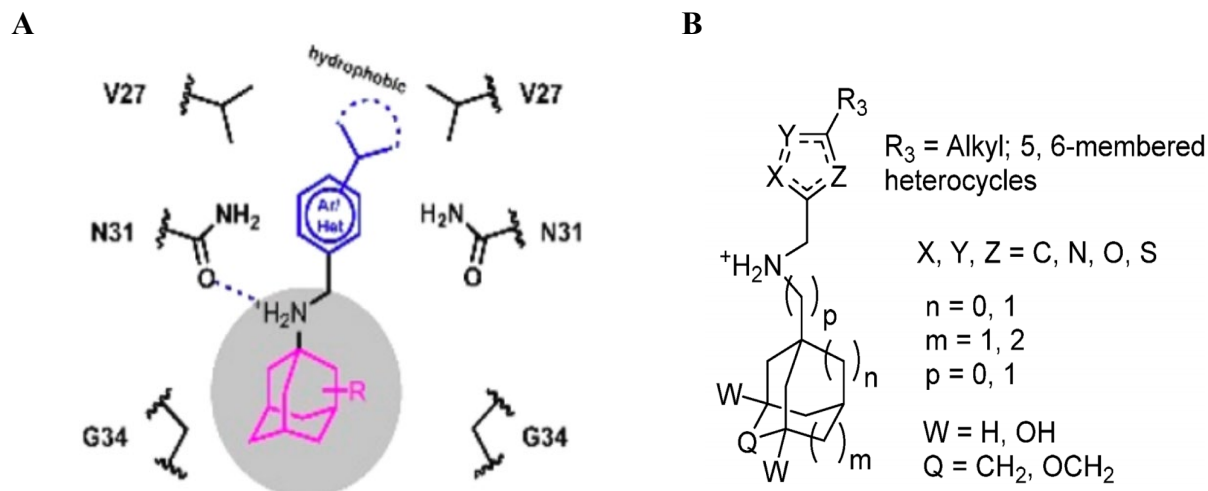


Figure 1.4. Design indicators and customizability of M2A-S31N inhibitors. (A) Pharmacophore of M2A-S31N Inhibitors. (B) Customizability options of foot scaffold and aryl body group.

X-ray diffraction to be oriented, like Amt, in the head-up position in the S31N mutant, the same orientation may not apply universally.¹⁷

Moving away from the strict Amt structure, many other opportunities for modification arise, allowing for fine-tuning of promising anti-influenza candidate drugs. Rimantadine derivatives can also take advantage of substitution off of the additional methylene bridge, which usually consists of another amine group that may or may not form a cyclized system with the primary amine. Similar derivatives can be formed by substituting Amt with other bulky ring-amine structures, such as derivatives of pinanamine, cyclooctylamine, spiropiperidine, and azocane.^{5,20} Substituted phenyl-amine systems may also serve as a viable alternative scaffold to Amt.²¹ Some promising activity has also been observed from linear polyamines, though they were excluded from this comparative study because their targeting of significantly different regions of M2A makes direct comparisons unmeaningful.²²

Though a vast library of compounds can be found focusing on the moieties shown in Figure

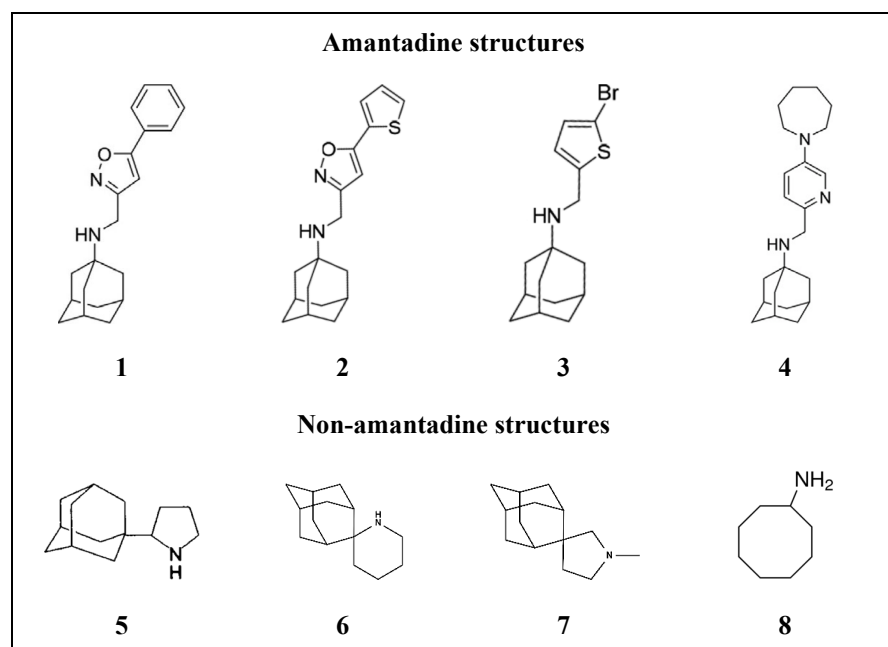


Figure 1.5. Parent compounds selected for comparison.

1.4, Figure 1.5 shows several parent compounds that were chosen for the comparative analysis to follow.^{5,16,17,20} Given the size constraints of M2A and the alternating hydrophobic and hydrophilic sections of its protein structure, even small changes can have a significant effect on a compound's efficacy. These compounds were compared with some of their derivatives as well as each other to identify factors that may provide better inhibition of M2A.

General selection criteria and synthesis techniques

Depending on the purpose of a specific study, several selection criteria were used. Studies focusing on design, synthesis, and *in vitro* or *in vivo* physiological effects often based their compound designs on a pharmacophore, such as that shown in Figure 1.4. While studies focusing on *in silico* techniques could form a compound list the same way, they most often employed online compound libraries. These groups formed learning sets on known inhibitors, such as Amt or promising candidates from recent studies, and searched for other compounds with similar therapeutic properties, which could show potential for repurposing a compound as an anti-influenza drug.

Some standard techniques to synthesize antiviral compounds are demonstrated in Figure 1.6. Formation of the functional structure, while rarely including very complicated techniques, can involve any number of common organic reactions, including substitution, cyclization, and reduction, as shown. Once the functional structure is formed, most of the reactions involved in these syntheses center around amine alkylation of an Amt or similar scaffold. Derivatives of Amt and other bulky, amine-containing scaffolds can be used to vary the structure and can be synthesized as needed, though most scaffolds and many of their derivatives are readily available commercially. After synthesis, compounds were characterized by ¹H-NMR, ¹³C NMR, and mass spectrometry.

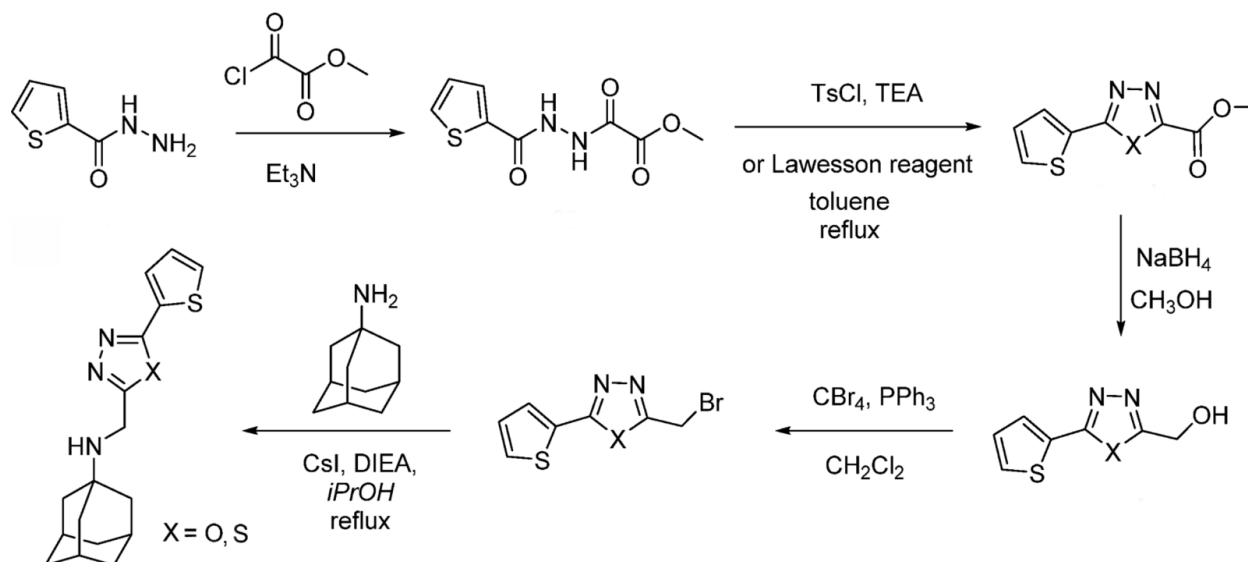


Figure 1.6. Example synthetic route to potential candidates for M2A-S31N inhibition.

Determination of antiviral properties

Channel inhibition was tested quantitatively by measuring conductance in a two-electrode voltage clamp (TEVC) assay using a frog oocyte with expressed M2A-S31N channels. Positive and negative baselines were established, following which conductance was measured after a 2 minute incubation period in a 100 μM solution of compound at pH 5.5. Inhibition was calculated as a percent of conductance reduction relative to the control values. The measurements were reported as the average of 3 assays performed with different oocytes. In general, block of greater than 75% was considered good for this study, and block of less than 50% was considered bad.

Plaque reduction assays were used to determine the half maximal effective concentration (EC_{50}) of compounds. Plaque assays were performed with MDCK cells infected with IVA-H1N1 possessing the M2A-S31N mutation, which were soaked in varying concentrations of the compounds for 45-72 hours. Plaque formation was measured as a titrated value of PFU/mL at several time intervals over the course of the assay. The EC_{50} was reported as the concentration at which plaque formation was reduced by 50% according to a best-fit growth curve relative to a

control with no compound. All assays were performed in duplicate. Ideally, EC₅₀ concentrations would be well into the sub-micromolar range.

To determine the 50% cytotoxic concentration (CC₅₀), MDCK cells at 50,000 cells/mL were soaked in an antibiotic growth medium for 24 hours in a 96-well cell culture plate. After the growth period, fresh medium containing varying concentrations of compound was added to the cells. After a 48-72 hour incubation period, the wells were stained with a colored or luminescent medium, and the absorbance was measured and normalized against wells containing cells only. CC₅₀ was reported as the concentration at which absorbance was at 50% according to a best-fit dose response curve with variable slope. The therapeutic index (TI) was then calculated by dividing the CC₅₀ by the EC₅₀ to estimate the window of therapeutic clearance. Values for TI greater than 100 were considered good.

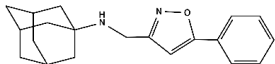
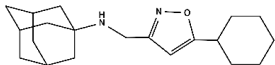
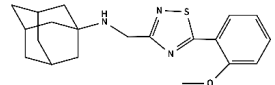
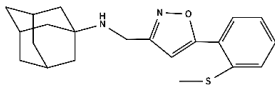
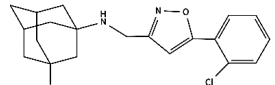
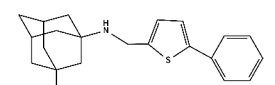
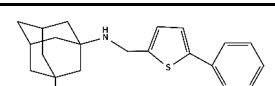
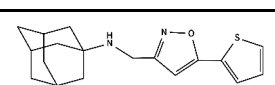
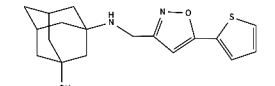
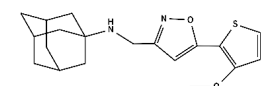
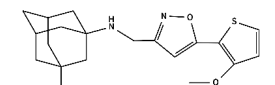
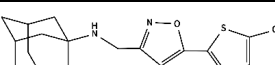
Compounds were introduced into mouse liver microsomes to test their physiological stability. Stability was measured as intrinsic liver clearance to determine removal of the compound by the liver. The stability was reported as the compound half-life (T_{1/2}) in minutes.

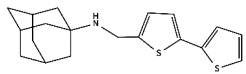
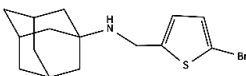
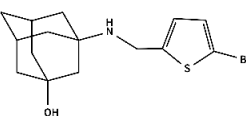
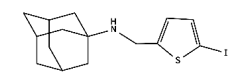
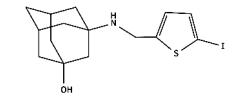
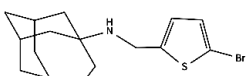
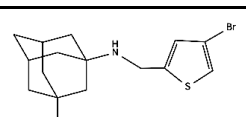
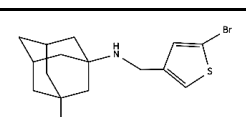
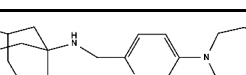
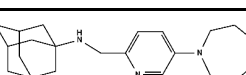
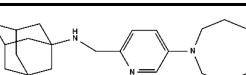
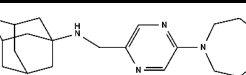
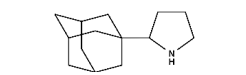
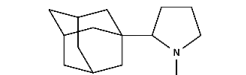
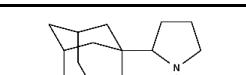
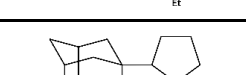
Comparison of chosen compounds

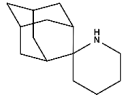
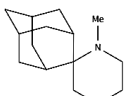
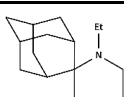
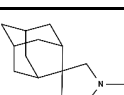
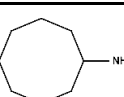
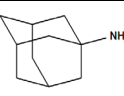
Derivatives of the parent structures **1-4** were chosen for comparison of M2A-S31N inhibition, efficacy, cytotoxicity, therapeutic index, and liver microsome stability, as available. Compound series **5-8** were chosen as examples of non-Amt scaffold structures for comparison of efficacy and toxicity, with compounds **7** and **8** being chosen for comparison with Amt in wild-type IVA. The parent structures and their derivatives can be found in Table 1.1 along with the available data for each as well as relevant data for Amt. Most structures can be thought of as a scaffold foot group, an aryl body group, and a hydrophobic head group. Derivatives differed

from their parent structures mainly in functional -OH groups on the scaffold and the size and functionality of the aryl and head groups.

Table 1.1. Compounds and derivatives for comparison of M2A S31N block, efficacy against IVA H1N1 M2A S31N, cytotoxicity, and liver stability.

Compounds		TEVC assay (% inhibition) M2A-S31N	EC ₅₀ (μmol/L) H1N1-S31N	CC ₅₀ (μmol/L) MDCK cells	Therapeutic Index ^a	T _{1/2} (min)
	1	91 ± 3	N.T.	N.T.	N.T.	N.T.
	1a	90 ± 3	N.T.	N.T.	N.T.	N.T.
	1b	59 ± 3	N.T.	N.T.	N.T.	N.T.
	1c	90 ± 2	1.2 ± 0.2	59.3 ± 2.6	49	N.T.
	1d	87 ± 1	N.T.	N.T.	N.T.	N.T.
	1e	84.6 ± 1.2	2.1 ± 0.2	80.5 ± 5.5	38	N.T.
	1f	78.7 ± 1.3	2.5 ± 0.8	65.2 ± 5.7	26	N.T.
	2	90.3 ± 3.4	0.3 ± 0.1	100	333	1.0
	2a	82 ± 2	N.T.	N.T.	N.T.	N.T.
	2b	81 ± 4	0.5 ± 0.2	30.6 ± 5.0	61	N.T.
	2c	85 ± 8	0.1 ± 0.04	> 200	> 2000	N.T.
	2d	78 ± 6	N.T.	N.T.	N.T.	N.T.

	2e	86.1 ± 1.2	12.16 ± 1.11	19.5 ± 2.0	1.6	N.T.
	3	76 ± 3	2.9 ± 0.8	123.2 ± 8.6	42	>145
	3a	65 ± 4	1.1 ± 0.2	238.1 ± 2.1	216	>145
	3b	79 ± 3	1.0 ± 0.1	70.2 ± 3.6	70	24.5
	3c	75.6 ± 1.2	0.9 ± 0.1	317.4 ± 12.0	353	>145
	3d	72.6 ± 1.4	0.6 ± 0.1	43.1 ± 2.8	72	9.1
	3e	56.6 ± 1.3	3.1 ± 0.3	380.7 ± 24.9	123	100.8
	3f	48.3 ± 0.5	5.1 ± 0.6	363.7 ± 18.3	71	N.T.
	4	74 ± 4	N.T.	N.T.	N.T.	N.T.
	4a	86 ± 2	N.T.	N.T.	N.T.	N.T.
	4b	81 ± 5	N.T.	N.T.	N.T.	N.T.
	4c	83 ± 4	N.T.	N.T.	N.T.	N.T.
	5	N.T.	77.3	274.1 ± 58.7 ^b	3.5	N.T.
	5a	N.T.	> 150	549.6	< 3.7	N.T.
	5b	N.T.	> 145	494.9 ± 30.6	< 3.4	N.T.
	5c	N.T.	15.4	284.1 ± 35.3	18	N.T.

	6	N.T.	> 170	452.9 ± 27.8 ^b	< 2.7	N.T.
	6a	N.T.	28.1	> 900 ^b	> 32	N.T.
	6b	N.T.	18.8	> 850 ^b	> 45	N.T.
	7	N.T.	0.5 ^c	N.T.	N.T.	N.T.
	8	N.T.	0.3 ^c	N.T.	N.T.	N.T.
	Amt	N.T.	0.3 ^c	> 1000	> 3333	N.T.

^aValues represent the quotient of mean CC₅₀ over mean EC₅₀ as an indicator of the therapeutic window. Values over 100 were considered good. ^bTested with CEM (human acute lymphoblastic leukemic) cells. ^cMinimum inhibitory concentration against IVA-WT. N.T. = not tested.

A lack of availability of truly analogous compounds made some comparisons difficult. For instance, the above comparison between **1** and **1a**, among many others, lacks conclusiveness as the only example found. The same can be said of the uniqueness of both the body and head groups of **1b**. A summary of several available observations is discussed below. Because data on M2A S31N inhibition was ubiquitously available for all compounds in series **1-4**, whereas other data was unavailable for many compounds, this summary will first focus on inhibition alone and then move to considerations of the efficacy, toxicity, and stability of the compounds.

Of the compounds chosen, **1** with its derivatives **1a-d**, **2a-d**, and **4** with its derivatives **4a-c** were studied by Musharrafieh and coworkers;¹⁶ **1e-f**, **2** with its derivative **2e**, and **3** with its derivatives **3a-f** were studied by Hu and coworkers;¹⁷ **5** with its derivatives **5a-c** and **6** with its derivatives **6a-b** were studied by Kolocouris and coworkers;²³ and **7** and **8** were studied by Yasushi Togo as well as Beare and coworkers.^{20,24}

Comparison of head groups

Series **1-4** contain head groups, while series **5-8** focus primarily on their foot groups. Of the first four series, the head groups are primarily phenyl homocycles, thiophenes, halides, and non-aryl heterocycles, respectively. Comparing inhibition of all four series to each other, the phenyl homocycle and thiophene compounds both contained several compounds that exhibited M2A-S31N inhibition above 90%, while none of the compounds of series **3** showed inhibition over 80% and series **4** contained only **4a** that performed well with 86% inhibition. Judging from these general observations, the best head groups for anti-M2A-S31N activity are phenyl and thiophenyl groups.

Of the phenyl homocycles, the unsubstituted phenyl and cyclohexyl rings (**1** and **1a**, respectively) performed very well, as did the methyl thioether (**1c**) and chlorine (**1d**), both of which were located on the α -carbon relative to the bridge. In contrast, the methyl ether (**1b**) fared particularly poorly, as was supported to a lesser degree by **2b** and **2c**. Between **1** and **1a**, only the aromaticity of the head group was different with equal inhibition, suggesting that the aromaticity of the head group played little part in the inhibitory effect of the compounds. Of course, the greater flexibility in a cyclohexyl vs phenyl ring could also play a role in the strength of hydrophobic interactions within the tight confines of the M2A-V27 cavity, but this is hard to support with any certainty without further examples or molecular dynamics simulations.

Comparing the compounds with thiophenyl head groups, there were no dramatically poor-performing compounds. As with compounds **1** and **1a**, the unsubstituted α -thiophenyl head group (**2** and **2e**) was a top performer even with different body groups, while ether-substituted head groups (**2b** and **2c**) performed more poorly. However, observation of **2a** and **2c** seems to suggest a small helping factor from the methyl ether, though the large uncertainty in the inhibition of **2c**

renders that conclusion dubious at best. Interestingly, though, **2d** showed a stark contrast to **1d**, as the chloro-substituted head group performed rather poorly. Owing to the behavior of the ether- and chloro-substituted groups, the thiophenyl head group, with its higher electron density, may be more susceptible to the influences of electron-donating and electron-withdrawing groups than the more stable phenyl head group despite the aromaticity of the ring seeming not to matter. The effect of positioning the halide substituent on the alpha-carbon relative to the bridge (**1d** and **1f**) versus the beta-carbon (**2b** and **2c**) was unable to be determined within the sample group, though.

The simple halide head group on the thiophenyl body group on **3** and **3b** performed comparably to the halo-substituted thiophenyl head group in **2d** despite its significantly different position on the molecule and, necessarily, within M2A. Comparing **3** with **3b** and **3a** with **3c**, the iodide substituent averaged higher than the bromide and was less affected by alcohol substitution on the foot group. Comparing **3** with **3e** and **3f**, with **3** having the sulfur at the alpha position to the bridge between the foot and body groups and the bromide on the beta carbon, **3e** having the bromide moved to the gamma carbon, and **3f** having the sulfur on the beta carbon and the bromide on the gamma carbon, both **3e** and **3f** showed dramatic decreases in channel inhibition.

The **4** series of compounds contained only two head groups: azepane in compounds **4**, **4a**, and **4c**, and azocane in compound **4b**. Between the analogous compounds **4** and **4b**, the bulkier azocane group displayed higher M2A inhibition, as could be expected for a homocycle interacting within a hydrophobic cavity, size constraints notwithstanding. Azocane's extra degree of freedom may also have allowed it to assume a better fit to interact with the M2A residues more efficiently. However, the margins of error between the two compounds overlapped too much for this to be considered a definitive result.

Comparison of body groups

Out of the compounds in series **1-4**, most of the chosen compounds had 2-azafuran (**1**, **1a**, **1c-d**, **2-2d**), thiophene (**1e-f**, **2e**, **3-3f**), or pyridine/pyrazine (**4** series) body groups. Of these, all of the 2-azafuran compounds exhibited moderate to good block, as did the thiophene compounds except those with only halide head groups. The pyridine body groups performed only moderately except with the addition of an alcohol on the foot group.

Between **1** and **1b**, the thiadiazole body group, rather than the ether on the head group, was probably the main factor that decreased the potency of **1b**. Because there was no direct analogue available for either the body or head group of **1b**, a definitive conclusion was difficult. However, considering that the methyl alpha ether on the head group **2b** caused a loss in block of only 9% compared to **2**, the difference of 32% block between **1** and **1b** suggests that the same addition was not to blame for the majority of the difference.

Direct comparisons of the 2-azafuran and thiophene body groups were possible by comparing **1d** with **1f** and **2** with **2e**. In both cases, the thiophene body group performed slightly lower in M2A inhibition than 2-azafuran. This pattern may indicate that the higher aromaticity afforded by the pyrrolic nitrogen and furanic oxygen may be beneficial compared to the lower aromaticity of the thiophenyl sulfur. In contrast, though, this trend is the opposite of that seen in the pyridine and pyrazine body groups. In comparing **4** and **4c**, the less-aromatic pyrazine outperformed the higher aromaticity of pyridine, casting doubt on aromaticity as a significantly contributing factor. Another possible trend that encompasses all three comparisons is that the number of hydrogen-bond acceptors, rather than the aromaticity, is the driving force for the increased M2A inhibition. The position of the body group within the N31 cluster supports the likelihood of this trend, as the amide side chain is capable of both accepting and donating hydrogen bonds. Because the amide

carbonyl accepts hydrogen bonding from the Amt nitrogen, a hydrogen bond could easily form between the amide nitrogen donor and any hydrogen-bond acceptors in the compound's body group. Such a hydrogen-bonding network has the potential to be enhanced by multiple acceptors, either due to bonding flexibility or through interactions with both the A30 and N31 residues, which are separated by about the same interspatial distance as the N-N distance in pyrazine.

Comparison of foot groups

The effect of a tertiary alcohol on the foot group is somewhat inconclusive. Comparison of **2** with **2a** and **3** with **3a**, both showed a fairly significant decrease (8.3% and 11%, respectively) in the compounds' inhibition of M2A-S31N. Doing the same with **3b** and **3c** showed a smaller decrease (3.4%), suggesting that the iodide head group was less affected than the bromide. However, comparing **2b** with **2c** and **4** with **4a** both show their inhibition increase (4% and 12%, respectively) with the addition of the alcohol. A conclusive argument cannot be made from a split among only five comparisons, especially with **2** and **2a-c** having the same body group and basic head groups. The uncertainty in **2b**, **2c**, and **4b** are large enough to make comparisons of their inhibition less meaningful; however, the large TI difference between **2b** and **2c** support the same conclusion without uncertainty issues, lending credence to the conclusion that the -OH was beneficial in **2c**. Further observation of the structures of these two groups might indicate that the combination of the foot alcohol group with a larger head group is beneficial where the alcohol combined with a smaller head group is detrimental.

Compound **3d** was analogous to compound **3** with one of the C—N-adjacent adamantyl methylenes replaced with an ethylene. **3d** averaged slightly lower than **3**, though their margins of error overlapped. Compound **3** also stands far ahead of **3d** when considering cytotoxicity and

liver stability, confirming that the normal, highly symmetrical structure of the adamantyl ring system stands out over the expanded structure in terms of drug candidacy.

Comparison of non-amantadine structures

While the compounds in series **5-8** all have non-amantadyl structures, all but compound **8** are very similar. Series **5** comprises cyclized rimantadine derivatives, series **6** comprises spiropiperidine derivatives of Amt, and compound **7** is a spiropyrrolidine derivative of rimantadine. Compound **8**, cyclooctylamine, is presented in its own group as the only non-adamantane scaffold for comparison with Amt.

Of series **5** and **6**, all of the compounds exhibited very low cytotoxicity. However, they also all displayed very low efficacy, causing all of their TI values to plummet. Interestingly for both series, a small substituent on the nitrogen was beneficial to cytotoxicity but detrimental to efficacy, but as the nitrogen's substituent was extended, the efficacy was greatly enhanced. Unfortunately for series **5**, the cytotoxicity also plummeted with the growing side chain. The same may be true for series **6**, but the cytotoxicity values, which had efficacy values approaching those in M2A-S31N that were comparable to Amt in M2A-WT, were large enough that the decrease may still have been acceptable. Of course, different nitrogen substituents could solve the cytotoxicity and efficacy problems, as the comparison in this sample set is far from exhaustive with only alkyl side chains considered.

Compounds **7** and **8** were compared directly with Amt. Only the efficacy was quantitatively provided for both compounds—showing values comparable to Amt—though compound **7** was reported to have no toxic or liver-damaging effects in human trials.²⁴ As for compound **8**, while a flat representation looks completely different than Amt, its flexible, eight-carbon ring folds to fill space very much like amantadine's rigid, ten-carbon ring system, allowing it to behave in much

the same way. The high efficacy and purportedly low toxicity of these compounds makes them possible scaffolds as well.

Efficacy, cytotoxicity, therapeutic index, and liver stability

Series **4** and compounds **7** and **8** had no EC₅₀ or CC₅₀ data given, and series **1**, **5**, and **6** lacked any compounds with a TI greater than 50. Of series **2**, **2** and **2c** showed high TI (333 and over 2000, respectively), with **2c** being the only compound in this study with a TI over 1000, putting its drug candidacy against M2A-S31N in a comparable position to Amt's drug response against M2A-WT. Compound **2** was quickly removed from the list of good compounds, though, because despite its high TI, its liver stability was extremely low, indicating that it would be unlikely to fare well in *in vivo* testing. Series **3** contained **3**, **3b**, and **3c** that exhibited good M2-S31N inhibition with **3a** and **3d** also showing decent inhibition, and it contained **3a**, **3c**, and **3e** that all exhibited good TI (216, 353, and 123, respectively). Compounds **3b** and **3d** were removed from consideration because of their lower TI (70 and 72, respectively).

Of the four compounds—**2c**, **3a**, **3c**, and **3e**—remaining for comparison of best traits, the series **3** compounds had microsomal liver stability values given. Of these, **3e** was the least likely candidate; though it exhibited the highest CC₅₀ (380.7 µmol/L) of series **1-4**, its EC₅₀ (3.1 µmol/L) was relatively high and its rather high stability (100.8 min) was still somewhat low relative to other candidates. Compounds **3a** and **3c** both exhibited higher TI than **3e**; though they displayed only borderline good EC₅₀ values (1.1 and 0.9 µmol/L, respectively), they shared the highest stability (>145 min) in the study. Unfortunately, the liver stability of **2c** was unavailable.

Because the effects of a scaffold alcohol group on M2A inhibition were inconclusive, its effects were examined by other data. Of the ten compounds with alcohols in their foot group, efficacy and toxicity data were available for seven (**1e**, **1f**, **2c**, **3a**, **3c**, **3e**, and **3f**), and

microsomal liver stability was given for three (**3a**, **3c**, and **3e**). EC₅₀ and TI varied wildly among the seven compounds, but the CC₅₀ values, interestingly, were all the highest reported in their respective groups. The liver stabilities of **3a** and **3c** were matched only by **3**, though, due to their values only being listed as being higher than the time limit of their particular study, a comparative analysis within those three compounds is impossible with current data. On the other hand, **3e**, a conformational analogue of **3a**, showed that the position of the bromide head group was indeed significant in terms of stability and efficacy in addition to channel inhibition.

Conclusions

Thirty-three compounds, tested previously by several research groups for M2A inhibition, were compared in an attempt to determine properties that increase or inhibit their efficacy as potential antivirals. For compound series **1-4**, variations in the adamantyl foot groups, aryl body groups, and cyclic head groups were considered. For series **5-6**, Amt derivatives with only an adamantyl foot group and an attached cyclic or spiro group were considered. Compounds **7** and **8** were compared with Amt in anti-M2-WT efficacy as other potential antiviral scaffolds.

The phenyl, cyclohexyl, thiophenyl, and azocanyl head groups by far performed the best out of series **1-4**. While oxygen was relatively unwelcome in the head group, sulfur fared much better. Halide substitution on the head group was benign in some cases and harmful in others, but it never appeared to be helpful and should probably be avoided. However, some of the compounds in series **3**, the head group of which was simply a halide, displayed very promising test results even though their M2A current inhibition was relatively low. Aromaticity of the head group appeared to make little to no difference, though bulkier head groups seemed to perform better. From these observations, the best head group would likely be a large, unsubstituted ring without restraints to its homo- or hetero-cyclic nature or its aromaticity.

The best body group was found to be an aryl heterocycle with 2 hydrogen-bond acceptors. The body groups that performed the best in this study were 2-azafuran and pyrazine. The foot group was tested with an alcohol group attached to a tertiary carbon and with the ring partially expanded. The alcohol group gave mixed results, but it appeared to be beneficial in conjunction with a large (substituted or larger than 6-membered) head group and disadvantageous when paired with a smaller head group. Further studies on the effect of the alcohol group would be beneficial to optimizing anti-IVA drug development. Ring expansion of the adamantane scaffold was detrimental in channel block, cytotoxicity, and liver stability; as such, the unmodified adamantyl moiety—alcohol substitution notwithstanding—was considered to be the best scaffold for the foot group for compounds containing an adamantane-like group.

While the rimantadine derivatives in series **5** showed dramatically worsening cytotoxicity with increasing side chain size, the spiropiperidine derivatives in series **6** seemed better suited to substitution. As only alkyl side groups were considered in this sample set, though, both scaffolds warrant tests with other body groups. Finding effective body groups for the spiropiperidine scaffold may be more difficult, however, due to the constrained geometry. Compounds **7** and **8** both showed efficacy comparable to Amt against M2-WT, showing that these two scaffolds have similar capabilities to Amt in wild-type IVA. Because the four scaffolds in series **5-8** present unique structures and geometries allowing for different customization options, they should be considered for development starting with similar modifications as those seen for Amt in the best practices listed above and optimizing from that point.

Future testing should be performed to refine available data of certain key points highlighted through this study. While azocane, the largest head group, performed well, no rings of higher than eight atoms entered the sample set, so research into larger rings should be performed to

determine optimal head group size. Series **4** compounds, particularly **4a**, should receive further testing for efficacy, toxicity, and, if available, microsomal liver stability to enhance comparisons further than only M2A current block, which by itself only contributes a small part to a holistic comparison. Compounds **3a** and **3c**—the most promising compounds in the study—should be strongly considered for proceeding into the next stages of drug development, as should **2c** pending stability testing.

References

1. Cheng, P. Y.; Palekar, R.; Azziz-Baumgartner, E.; Iuliano, D.; Alencar, A. P.; Bresee, J.; Oliva, O.; de Souza, MDM; Widdowson, M. A. *Influenza Other Respir. Viruses* **2015**, *9*, Suppl 1:13-21.
2. Osterholm, M. T. *New Engl. J Med.* **2005**, *352*, 1839-1842.
3. Chan, M. B. *World Health Organ.* **2006**, *84*, 9-10.
4. Seetoh, T.; Liverani, M.; Coker, R. *Glob. Public Health* **2012**, *7*, 717-730.
5. Wu, X.; Wu, X.; Sun, Q.; Zhang, C.; Yang, S.; Li, L.; Jia, Z. *Theranostics* **2017**, *7*, 826-845.
6. Skehel, J. J.; Hay, A. J.; Armstrong, J. A. 1978. *J. Gen. Virol.* **1978**, *38*, 97-110.
7. Thomaston, J. L.; Wu, Y.; Polizzi, N.; Liu, L.; Wang, J.; DeGrado, W. F. *J. Am. Chem. Soc.* **2019**, *141*, 11481-11488.
8. Liang, R.; Swanson, J. M. J.; Madsen, J. J.; Hong, M.; DeGrado, W. F.; Voth, G. A. *Proc. Natl. Acad. Sci. U.S.A.* **2016**, *113*, E6955-E6964.
9. To, J.; Torres, J. *Cells* **2019**, *8*, 654.
10. Okada, A.; Miura, T.; Takeuchi, H. *Biochemistry* **2001**, *40*, 6053-6060.
11. Agmon, N. *Chem. Phys. Lett.* **1995**, *244*, 456-462.
12. Wang, C.; Takeuchi, K.; Pinto, L. H.; Lamb, R. A. *J. Virol.* **1993**, *67*, 5585-5594.
13. Llabrés, S.; Juárez-Jiménez, J.; Masetti, M.; Leiva, R.; Vásquez, S.; Gazzarrini, S.; Moroni, A.; Cavalli, A.; Luque, F. J. *J. Am. Chem. Soc.* **2016**, *138*, 15345-15358.
14. Sakai, Y.; Kawaguchi, A.; Nagata, K.; Hirokawa, T. *Microbiol. Immunol.* **2018**, *62*, 34-43.
15. Bright, R. A.; Shay, D.; Bresee, J.; Klimov, A.; Cox, N; Ortiz, J. *Morb. Mortal. Wkly. Rep.* **2006**, *55*, 44-46.
16. Musharrafieh, R.; Ma, C.; Wang, J. *Eur. J. Pharm. Sci.* **2020**, *141*, 105124.
17. Hu, Y.; Hau, R. K.; Wang, Y.; Tuohy, P.; Zhang, Y.; Xu, S.; Ma, C.; Wang, J. *ACS Med. Chem. Lett.* **2018**, *9*, 1111-1116.
18. Li, F.; Ma, C.; DeGrado, W. F.; Wang, J. *J. Med. Chem.* **2016**, *59*, 1207-1216.
19. Ottiger, P.; Pfaffen, C.; Leist, R.; Leutwyler, S. *J. Phys. Chem. B* **2009**, *113*, 2937-2943.
20. Togo, Y. *Antimicrob. Agents Ch.* **1973**, *4*, 641-642.

21. Radošević, D.; Sencanski, M.; Perović, V.; Veljković, N.; Prljic, J.; Veljković, V.; Mantlo, E.; Bukreyeva, N.; Paessler, S.; Glisic, S. *Front. Cell. Infect. Microbiol.* **2019**, *9*, 67.
22. Lin, T.; Heider, H.; Schroeder, C. *J. Gen. Virol.* **1997**, *78*, 767-774.
23. Kolocouris, N.; Kolocouris, A.; Foscolos, G. B.; Fytas, G.; Neyts, J.; Padalko, E.; Balzarini, J.; Snoeck, R.; Andrei, G.; Clercq, E. D. *J. Med. Chem.* **1996**, *39*, 3307-3318.
24. Beare, A. S.; Hall, T. S.; Tyrrell, D. A. J. *Lancet*, **1972**, *299*, 1039-1040.

CHAPTER 2

Introducing Copper into the Arena of Influenza A M2 Inhibitors Using Net Neutral Complexes with Acid and Amide Chelation

Gordon, N. A.; McGuire, K. L.; Wallentine, S. K.; Mohl, G. A.; Lynch, J. D.; Harrison, R. G.; Busath, D. D. Divalent copper complexes as influenza A M2 inhibitors. *Antiviral Res.* **2017**, *147*, 100-106.

McGuire, K. L.; Hogge, J.; Hintze, A.; Liddle, N.; Nelson, N.; Pollock, J.; Brown, A.; Facer, S.; Walker, S.; Lynch, J.; Harrison, R. G.; Busath, D. D. Copper Complexes as Influenza Antivirals: Reduced Zebrafish Toxicity. In *Engineered Nanomaterials – Health and Safety*; Avramescu, S. M., Ed.; IntechOpen: London, 2020; Ch. 9.

I hereby confirm that the use of this article is compliant with all publishing agreements.

Abstract

New M2 blockers effective against the ubiquitous amantadine-resistant S31N M2 mutation in influenza A are needed. Six copper complexes, **2**, **4**, **6**, **8**, **9**, and **10**, were synthesized and found to block both wild type and S31N M2. Free Cu²⁺ also blocks M2-S31N but not S31N/H37A. The copper complexes do not block M2-H37A (either S31 or S31N). The complexes were effective against three influenza A strains in cell-culture assays, but less toxic to cells than CuCl₂. For example **4**, Cu(cyclooctyliminodiacetate), which was stable at pH > 4 in the buffers used, had an EC₅₀ against A/Calif/07/2009 H1N1 of 0.7 ± 0.1 μM with a CC₅₀ of 147 μM (therapeutic index, averaged over three strains, 67.8). In contrast, CuCl₂ had an EC₅₀ of 3.8 ± 0.9 μM and CC₅₀ of 19 μM (therapeutic index 5.0). Because M2-H37 is highly conserved, these complexes show promise for further testing as drugs against all strains of influenza A.

1. Introduction

The release of ribonucleoproteins from M1 upon fusion of the influenza A envelope to the endosomal membrane and protection of nascent hemagglutinin from premature acidification in the trans-Golgi of infected cells are both mediated by the viral proton transporter, M2.^{1,2} Native

(WT) M2 is a well-established antiviral target for the M2 channel blockers amantadine and rimantadine,³⁻⁶ but the M2-S31N and other nearby mutations, (L26F, V27A/T/S, A30T, and G34E) are known to cause insensitivity to amantadine *in vitro*.^{7,8} Because the S31N mutation is now nearly universal in human infections,⁹ amantadine and rimantadine are no longer useful therapeutics.¹⁰ Several attempts have been made to identify variants of these drugs and others that could block the S31N mutation and/or other amantadine resistance mutations. For instance, isoxazole-adamantane¹¹ and pinanamine¹² compounds effectively block M2-S31N, spiranamine blocks M2 L26F, V27A, and WT,¹³ and benzyl substituted amantadines are active against both the WT and S31N mutant.¹⁴ However, they are all limited in the scope of M2 variants they block. This led us to explore an approach using metals that could, in theory, target all functional forms of M2, perhaps in most or all amantadine-sensitive and -resistant strains.

The homotetrameric M2 channels are exquisitely selective for transport of H^+ over other monovalent ions⁵ due to a tightly-packed cluster of His37 side chains at the narrowest passage in the channel.^{15,16} This residue is highly conserved in influenza A (99.97% identical in all isolates found in GenBank). The M2 current in transfected oocytes was found previously to be blocked by 250–500 μM Cu^{2+} , with block eliminated by mutation of M2-His37 to Ala.¹⁷ Cu^{2+} and other divalent cations Ni^{2+} , Pt^{2+} , Cd^{2+} , Mg^{2+} , Mn^{2+} , and Zn^{2+} caused only partial, readily reversible block at 1–2 mM concentrations. Using triangulation of paramagnetic shielding effects in solid-state NMR, Cu^{2+} was found to bind in the core of the His37/Trp41 cluster located within the homotetramer.¹⁸

Metals have a long history of medicinal applications, beginning primarily in 1978 with the approval of cisplatin as an anticancer drug.¹⁹ While much medicinal metal-complex research attempted to mimic the anticancer success of cisplatin,²⁰⁻²⁴ many uses for metal complexes have

been discovered for other conditions. Gold, as a noble metal, was discovered to be effective in controlling the progression of arthritis as early as 1934,²⁵⁻²⁷ vanadium aided patients with diabetes as an insulin-mimetic drug,²⁸ and zinc was researched as a chemokine receptor antagonist with anti-HIV activity and as a stem-cell mobilizer.²⁹

A great deal of copper-related medicinal research centered around chelation therapy to remove excess copper from the body to treat Alzheimer's and Wilson's diseases,^{30,31} including, interestingly, zinc chelates³² and a complex anion of molybdenum.³³ Non-removal applications existed in the literature as well, however, as evidence was shown that at least one potential Alzheimer's disease drug acted as a copper transporter to correct the faulty copper homeostasis in the brain rather than removing the copper (Bush 2008, Ferrada 2007, Atwood 2000, Treiber 2004),^{30,34-36} and a copper(II)-bis-histidine complex was utilized to deliver copper to human serum albumin, counteracting deficiencies in Menkes disease patients.³⁷ Recently, copper complexes have also been developed as anti-inflammatory, antibiotic, and chemotherapeutic agents.³⁸⁻⁴⁵ Though *in vivo* side-reactions with non-target binding sites must be especially considered during drug development for metal complexes,⁴⁶ treating patients with metal-chelate complexes can mitigate that danger.³⁷

Although intracellular copper levels are tightly regulated,^{47,48} daily dietary intake limitations are modest,⁴⁹ such that the bodily exposure to the copper content from moderate doses of such therapeutics by traditional routes can be expected to be well tolerated. By derivatizing the amines of known M2 blockers, amantadine (Amt) and cyclooctylamine (CO), to form the iminodiacetate or iminodiacetamide, we have synthesized Cu²⁺ containing complexes and characterized them by NMR, IR, MS, UV-vis, and inductively coupled plasma mass spectroscopy (ICP-MS). These can be compared with other small molecule inhibitors of M2-S31N transport.^{50,51} Because Cu²⁺

binds strongly to imidazole, it was suggested that the Cu^{2+} complexes also block M2 through His37-imidazole binding. In addition, the His37 cluster is highly conserved in nature,⁵² making it a prime target in the M2 channel.

Drawing from the observation that divalent cations, particularly copper, block M2 current¹⁷ binding in the His37-Trp41 side chain quadruplex,¹⁸ divalent copper complexes of Amt were synthesized and found to be effective influenza A inhibitors with reduced cytotoxicity compared to CuCl_2 . The copper ligands developed were based on Amt and the lesser-known, equally effective M2-WT blocker, CO,^{53,54} and extended via the amine with the functional groups iminodiacetate or iminodiacetamide. Six Cu^{2+} complexes (Figure 2.1) were synthesized and characterized using NMR, IR, MS, UV-Vis, and ICP-MS. Proton current block and H37 specificity were tested in two electrode voltage-clamp studies, and cytotoxicity and efficacy were tested in cell cultures. Three-day solution stability studies were performed with the Amt- and CO-containing complexes **2**, **4**, **6**, and **8** in each of water and both biological testing media. Complexes **2** and **4** in particular stood out as promising examples of metal complexes in the arena of M2 inhibition.

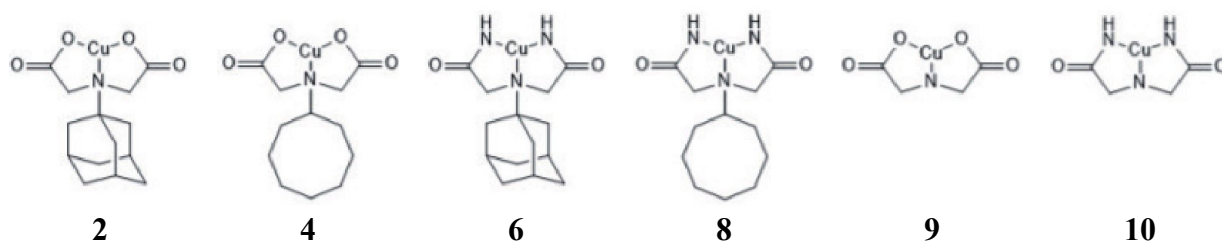


Figure 2.1. Copper complexes with the functional groups iminodiacetate or iminodiacetamide extended via the amine to either AMT or CO.

2. Materials and methods

2.1. Instruments and materials

Solvents and compounds were used as received by commercial suppliers. Purity of tested complexes was verified by ^1H -NMR, ICP and elemental analysis and found to be $\geq 95\%$. The copper complexes were usually accompanied by two water molecules, but in some cases the number of waters varied between batches and was quantified before running assays with the complexes. The IDAA complexes contained NaCl, which was quantified before doing assays. NaCl was verified by x-ray photoelectron spectroscopy. The hydrated complexes lost water during the melting point measurements but did not melt.

^1H and ^{13}C NMR spectra were recorded on Varian 300 and 500 MHz multinuclear FT-NMR spectrometers. Proton chemical shifts were reported in parts per million (δ) with reference to tetramethylsilane (TMS, δ 0.0 ppm) or their respective solvent peaks. Mass measurements were done on an Agilent model G1969A LC/MSD TOF mass spectrometer. IR spectra were collected on a Thermo Scientific Nicolet iS5 FTIR using Nujol. Elemental analysis was done by M-H-W Laboratories. UV-Vis studies were done on a HP 8453 spectrophotometer. Copper contents were confirmed by inductively coupled plasma mass spectrometry done on a Perkin Elmer Optima 2000 OES spectrometer. X-ray diffraction data comprising φ - and ω - scans were collected using a MACH3 four circle diffractometer coupled to a Bruker Apex II CCD detector with a Bruker-Nonius FR591 rotating anode X-ray source producing Cu K_α radiation ($\lambda = 1.54178 \text{ \AA}$). X-ray photoelectron spectroscopy (XPS) analyses were performed by using a Surface Science SSX-100 X-ray photoelectron spectrometer.

2.2 Compound and complex synthesis

2.2.1. Synthesis of N-(1-adamantyl)-iminodiacetic acid (**1**)

This compound was synthesized by a revised procedure from that found in the literature.⁵⁵ Amantadine (9.068 g, 60 mmol) and bromoacetic acid (18.569 g, 134 mmol) were added to a 50:50 ethanolic aqueous mixture (100 mL) in a 2:1 molar ratio that was then titrated to pH = 11.5 using 12 M NaOH. The mixture was refluxed at 93 °C for 21 h while maintaining an alkaline pH > 11. The ethanolic aqueous mixture was extracted with diethyl ether three times (30 mL each) to remove organic impurities. Following extraction and removal of the organic phase, the aqueous phase was titrated to pH 3 with concentrated HCl. Slow evaporation in 50:50 EtOH:H₂O afforded the desired white precipitate. Yield: 7.847 g (49.0%). ¹H NMR (500 MHz, MeOH-d₄, 25 °C): δ 3.89 (s, 4H), 2.21 (s, 3H), 1.97 (s, 6H), 1.73 (t, 6H) ppm. ¹³C NMR (500 MHz, MeOH-d₄, 25 °C): δ 170.4, 81.4, 65.4, 52.6, 46.9, 35.5, 30.1, 20.5, 12.5 ppm. HRMS (ESI): m/z calc for C₁₄H₂₁NO₄ + H⁺: 268.15; found 268.14. Selected IR frequencies (cm⁻¹): 3364 (COOH), 1614 (CO). Decomposed at 220 °C.

2.2.2. Synthesis of Copper N-(1-adamantyl)-iminodiacetic acid (**2**)

Copper acetate monohydrate (0.2004 g, 1.0 mmol) was dissolved in 75 mL of methanol. Separately, **1** as prepared above (0.6148 g, 1.0 mmol) was dissolved in 50 mL of methanol, and the resulting solution was added to the copper acetate solution with stirring. As the solutions were combined, the color changed from aqua to blue. After 5 minutes, 250 mL of diethyl ether was added, and the layers were allowed to mix slowly for 5 hours. The light blue precipitate was collected by filtration and rinsed with 125 mL of diethyl ether, which was added to the filtrate. The process of filtering and adding diethyl ether was repeated to collect two more crops. Yield: 0.2203 g (60.2% yield of dihydrate complex). Crystals can be obtained from water by slow

evaporation. ^1H NMR (500 MHz, MeOH-d_4): no compound peaks. ^1H NMR (500 MHz, MeOH-d_4 , 1 drop TFA): δ 4.19 (s, 4H), 2.24 (s, 3H), 2.01 (s, 6H), 1.73 (t, 6H) ppm. HRMS (ESI): m/z calculated for $[\text{Cu}(\text{C}_{14}\text{H}_{19}\text{NO}_4)\cdot\text{H}_2\text{O}]^+$: 346.07; found 346.09. Selected IR frequencies (cm^{-1}): 1592(CO). Elemental analysis calculated for $\text{Cu}(\text{C}_{14}\text{H}_{19}\text{NO}_4)\cdot 2\text{H}_2\text{O}$: C, 46.08; H, 6.35; N, 3.84; found: C, 46.20; H, 6.38; N, 3.73. Decomposed at $> 250\text{ }^\circ\text{C}$.

2.2.3. Synthesis of Cyclooctyliminodiacetic acid (3)

Cyclooctylamine (0.3956 g, 3.1 mmols) was added to a mixture of water (4 ml) and ethanol (25 ml). Bromoacetic acid (0.8641 g, 6.2 mmols) was added. The solution was titrated to pH 11 with 12 M sodium hydroxide, and maintained at that pH. The solution was refluxed and stirred for 24 hours. The reaction mixture was cooled to $0\text{ }^\circ\text{C}$ and a beige precipitate was collected by vacuum filtration and washed with 10 mL of ethanol. The filtrate was cooled to $0\text{ }^\circ\text{C}$ and allowed to sit for 20 minutes. The beige precipitate that formed was collected by vacuum filtration and washed with 10 ml of ethanol. Acetonitrile (30 ml) was added to the filtrate. A precipitate formed, was filtered, and discarded. The filtrate was allowed to sit for several days, and a beige precipitate formed. The precipitate was collected. The combined beige precipitates were air-dried, weighed 0.7097 g (79.5% of disodium compound), and produced the sodium salt of **3**. ^1H -NMR (D_2O , 300 MHz) δ ppm: 3.11 (s, 4, CH_2), 2.88 (t, 1, CH), 1.59 (m, 4, CH_2), 1.41 (m, 4, CH_2), 1.31 (m, 6, CH_2). ^{13}C NMR (D_2O , 500 MHz) δ = 178.0, 61.1, 55.1, 28.9, 25.9, 25.6, 24.9 ppm. HRMS (ESI) m/z : calculated for $[\text{C}_{12}\text{H}_{21}\text{NO}_4 + \text{H}^+]$ 244.15; found 244.15. Selected IR frequencies (cm^{-1}): 1622 (CO), 1600 (CO). Decomposed at $260\text{ }^\circ\text{C}$.

2.2.4. Synthesis of Copper cyclooctyliminodiacetic acid (4)

Copper acetate monohydrate (0.1434 g, 0.72 mmols) was added to 20 ml of methanol, disodium cyclooctyliminodiacetate (0.2064 g, 0.72 mmols) was added to it and the solution was

stirred for 5 minutes. As **3** dissolved, the solution became dark blue. The solution was allowed to evaporate for several days while blue-green solid formed. When 2 mL of methanol remained, the solid was collected by decantation, dried, and gave 0.2860 g (89.7% yield of hexahydrate complex with 0.5 acetic acids). $^1\text{H-NMR}$ (MeOD, 300 MHz) δ broad peaks from 3.67-1.19. $^1\text{H-NMR}$ (MeOD, 1 drop TFA, 300 MHz) δ 4.10 (s, 4H); 3.55 (s, 1H); 1.88 (b, 4H); 1.68 (b, 4H); 1.5 (b, 4H); 1.42 (b, 2H). HRMS (ESI) m/z : calculated for $[\text{Cu}(\text{C}_{12}\text{H}_{19}\text{NO}_4) + \text{COOH} + \text{H}^+]$ 351.01; found 351.080. Selected IR frequency (cm^{-1}): 1590 (CO). Elemental analysis calculated for $\text{Cu}(\text{C}_{12}\text{H}_{19}\text{NO}_4) \cdot 2.5\text{H}_2\text{O} \cdot 0.5\text{CH}_3\text{COOH}$: C, 41.10; H, 6.90; N, 3.69; found: C, 41.26; H, 5.63; N, 4.01. Decomposed at $> 250\text{ }^\circ\text{C}$.

2.2.5. Synthesis of Amt-iminodiacetamide (**5**)

Amantadine (0.3169 g, 2.10 mmol) and bromoacetamide (0.5783 g, 4.19 mmol) were dissolved in 10 ml of DMF. Diisopropylethylamine (0.6769 g, 5.23 mmol) was added to the solution. The reaction was allowed to stir at room temperature for two hours followed by four hours at $115\text{ }^\circ\text{C}$. The white precipitate that formed was collected and washed with 6 ml DMF, 8 ml of water, and 4 ml of methanol. The reaction gave 0.3846 g of product (69.2%). $^1\text{H-NMR}$ (DMSO, 500 MHz) δ 7.97 (s, 2H), 6.99 (s, 2H), 3.09 (s, 4H), 2.00 (s, 3H), 1.56(m, 12H) ppm. $^{13}\text{C NMR}$ (DMSO, 500 MHz) δ 175.9, 55.0, 54.1, 38.7, 36.4, 29.2 ppm. HRMS (ESI) m/z : calculated for $\text{C}_{14}\text{H}_{23}\text{N}_3\text{O}_2 + \text{H}^+$: 266.187; found 266.185. Selected IR frequencies (cm^{-1}): 3320(NH), 3154(NH), 1693(CO), 1667(CO). Decomposed at $290\text{ }^\circ\text{C}$.

2.2.6. Synthesis of Cu(Amt-iminodiacetamide) (**6**)

5 (0.0907g, 0.34 mmol) was added to 20 ml of dry DMF under N_2 . Sodium hydride (0.0310 g, 0.78 mmol) in 5 ml of dry DMF was added to the **5** solution over a five minute period. Copper chloride dihydrate (0.0582 g, 0.34 mmol) was dissolved in 5 ml of dry DMF and quickly added.

The reaction was stirred overnight at room temperature under N₂. THF (75 mL) was added and a purple precipitate formed. The precipitate was filtered, washed with 10 ml of ethanol and 15 ml of diethyl ether. The reaction gave 0.0644 g of product (37.2% yield of dihydrate sodium chloride complex). ¹H-NMR (DMSO, 500 MHz) δ ppm: no compound peaks. ¹H-NMR (DMSO, TFA, 500 MHz) δ ppm: 7.97 (s, 2H), 6.99 (s, 2H), 3.09 (s, 4H), 2.00 (s, 3H), 1.56 (m, 12H). HRMS (ESI) m/z: calculated for [Cu(C₁₄H₂₁N₃O₂) + H⁺] 327.09; found 327.10. Selected IR frequencies (cm⁻¹): 1665(CO), 1571(CO). Elemental analysis calculated for Cu(C₁₄H₂₁N₃O₂)·2H₂O·2.5NaCl: C, 33.04; H, 4.95; N, 8.36; found: C, 32.96; H, 4.45; N, 8.37. Decomposed at > 250 °C.

2.2.7. Synthesis of Cyclooctylimidodiacetamide (7)

Cyclooctylamine (0.7715 g, 6.0 mmol) and 1.6896 g (12.2 mmol) bromoacetamide were dissolved in 20 ml of acetonitrile. Anhydrous K₂CO₃ 1.8455 g (13.3 mmol) was added. The mixture was stirred and heated at 60 °C for 16 hours and allowed to cool. The flask was sonicated to remove any solid adhered to the glass and the tan precipitate was filtered off; the filtrate was set aside and the precipitate was washed with water. The solid and the filtrate were combined and heated to reflux; the solution became transparent. This solution was allowed to cool and the resulting colorless crystals were collected by vacuum filtration. The product weighed 0.9702 g (66.3%). ¹H-NMR (DMSO, 300 MHz) δ 7.72(s, 2H), 7.17(s, 2H), 2.92(s, 4H), 2.58(m, 1H), 1.70 (m, 4H), 1.52 (m, 4H), 1.46 (m, 6H). ¹³C NMR (DMSO, 500 MHz) δ 173.8, 61.0, 55.6, 29.9, 26.39, 26.31, 25.5 ppm. HRMS (ESI) m/z: calculated for [C₁₂H₂₃N₃O₂ + H⁺]: 242.16 ; found 242.186. Selected IR frequencies (cm⁻¹): 3317 (NH), 3163 (NH), 1690 (CO), 1665 (CO). Melting point 152-154°C.

2.2.8. Synthesis of Copper cyclooctylimidodiacetamide (8)

7 (0.8162 g, 3.4 mmol) was dissolved in 150 mL dry DMF under nitrogen. NaH (0.3094 g, 7.735 mmol) was added, and the solution was stirred for 5 minutes. Separately, CuCl₂·2H₂O (0.5983 g, 3.5 mmol) was dried in an oven for several hours at 120° C, cooled in a desiccator, and dissolved in 100 mL dry DMF. The gold CuCl₂ solution was then poured into the **7** solution. The solution's color started green and gradually turned dark blue. The solution was stirred at room temperature for 16 hours under nitrogen. The solution was then removed from nitrogen and 500 mL THF was added to it. The dark blue precipitate that formed was collected by filtration, rinsed with THF, and dried *in vacuo*. Yield: 0.7356 g (37.8% of dihydrate sodium chloride complex). ¹H-NMR (CD₃OD, 500 MHz): broad signals. ¹H-NMR (CD₃OD, 1 drop TFA, 500 MHz) δ 4.00(s, 4H), 3.51(m, 1H), 1.87 (m, 4H), 1.72 (m, 4H), 1.52 (m, 6H). HRMS (ESI negative) m/z: calculated for [CuC₁₂H₂₁N₃O₂ + H₂O + OH⁻]: 337.11; found 337.126. Selected IR frequencies (cm⁻¹): 1594(CO). Elemental analysis calculated for Cu(C₁₂H₂₁N₃O₂)·2H₂O·4NaCl: C, 25.17; H, 4.40; N, 7.34; found: C, 24.62; H, 4.21; N, 7.13. Decomposed at > 250 °C.

2.2.9. Synthesis of Copper iminodiacetic acid (9)

This complex was previously made by a different procedure.⁵⁶ Iminodiacetic acid (0.2455 g, 1.84 mmol) was dissolved in 25 ml of water and copper(II) acetate monohydrate (0.3682 g, 1.84 mmol) was added to the solution. The solution was sonicated until all of the copper acetate dissolved. NaOH (12 M) was added to the solution until the pH reached 7. The flask was allowed to stand at room temperature for 24 hours during which time a precipitate formed. The blue precipitate was collected by filtration and weighed 0.2887 g (68.0% yield of dihydrate complex). ¹HNMR (300 MHz, D₂O) no compound peaks ¹HNMR (300 MHz, D₂O, TFA) δ 3.82 (s). HRMS (ESI): m/z calc for Cu(C₄H₅NO₄) + H⁺: 194.959; found 194.95. Selected IR frequencies (cm⁻¹):

3169 (NH), 1590 (CO). Elemental analysis calculated for $\text{Cu}(\text{C}_4\text{H}_5\text{NO}_4) \cdot 2\text{H}_2\text{O}$: C, 20.83; H, 3.93; N, 6.07. Found: C, 21.22; H, 3.77; N, 5.69. Decomposed at $> 250^\circ\text{C}$.

2.2.10. Synthesis of Copper iminodiacetamide (10)

To 25 ml of dry DMF under N_2 was added 2-[(carbomoylmethyl)amino]acetamide (0.2600 g, 1.98 mmol). Sodium hydride (0.1790 g, 4.47 mmol) in 5 ml of dry DMF was added to the solution and it was allowed to stir for five minutes. Copper chloride dihydrate (0.3379 g, 1.98 mmol) dissolved in 5 ml of dry DMF was quickly added and the solution stirred for 16 hours at room temperature. THF (100 ml) was added to the reaction mixture and the resulting green precipitate was collected by filtration and centrifugation. After drying under vacuum, the remaining solid weighed 0.1866 g (23.3% yield of dihydrate complex with sodium chloride). ^1H NMR (300 MHz, DMSO) δ no compound peaks. ^1H NMR (300 MHz, DMSO, TFA) δ 7.80 (s, 2H), 7.52 (s, 2H), 3.69 (s, 4H). HRMS (ESI): m/z calc for $\text{Cu}(\text{C}_4\text{H}_7\text{N}_3\text{O}_2) + \text{H}^+$ 192.99; found 192.998. Selected IR frequencies (cm^{-1}): 1663 (CO). Elemental analysis calculated for $\text{Cu}(\text{C}_4\text{H}_7\text{N}_3\text{O}_2) \cdot 2\text{H}_2\text{O} \cdot 3\text{NaCl}$: C, 11.89; H, 2.74; N, 10.40. Found: C, 12.32; H, 2.28; N, 9.79. Decomposed at $> 250^\circ\text{C}$.

2.3. Stability Studies

Solutions of the complexes were made by dissolving a few milligrams of complex in 3.0 mL of solvent to make 10 mM solutions. Complexes **2**, **6**, and **8** were dissolved in methanol, and **4** was dissolved in water. The solutions were sonicated and gently warmed to aid dissolution. 100 μL of each solution was then added to 9.90 mL of either water, Barth's or simple electrolyte medium (SEM: 148 mM NaCl, 3 mM KCl, 1.6 mM CaCl_2 , 0.8 mM MgCl_2 , 0.75 mM Na_2HPO_4 , 0.1 mM NaH_2PO_4 , pH 7.2 to make 100 μM solutions and the solutions were capped). UV-vis

spectra were taken at time increments over three days at room temperature and background subtraction of solvent was applied.

2.4. Electrophysiology

Oocytes from *Xenopus laevis* (Ecocyte, Austin, TX) were prepared with A/Udorn/72 H3N2, A/Udorn/72 H3N2 M2-S31N, or A/Udorn/72 H3N2 M2-S31/ H37A mRNA and maintained at 4 °C and pH 7.4 for 72 hours, at which time electrophysiological recording was performed. Whole-cell currents were recorded with a two-electrode voltage-clamp apparatus at $V_m = -20$ mV, room temperature, in Barth's solution, pH 7.5. Inward current was induced by perfusion with Barth's pH 5.3. Percentage block of the original inward current by 100 μ M test compound or complex was measured just before washout, which was done 8 min 50 s after drug exposure, or upon current stabilization, for each compound or complex.

2.5. Cell culture

Influenza-sensitive Madin-Darby canine kidney (MDCK, ATCC, Manassas, VA) cells were grown in Dulbecco's Modified Eagle Medium (DMEM, Sigma-Aldrich, St. Louis, MO). 1.1 g/L of sodium bicarbonate, 10 μ M Hepes, 100 U/mL of Penicillin and 100 μ g/mL of Streptomycin were added to the growth and cytotoxicity test media. Cell cultures were incubated at 37 °C in a humidified 5% CO₂ incubator. Passaging was carried out twice weekly using 0.25% trypsin-EDTA (ThermoFischer Scientific, Waltham, MA). The growth medium was supplemented with 5% fetal bovine serum (FBS, Hyclone, Logan, UT).

2.6. Cytotoxicity assay

MDCK cells were seeded into the 60 internal wells of a 96-well plate at a density of 2×10^4 cells/well in 5% FBS DMEM. After 48 h, growth media was removed, and replaced with DMEM supplemented with 1% FBS containing test complex at concentrations of 4 μ M to 1 mM in 2-

fold increments, six wells per concentration. Six wells without the test compound or complex served as controls. The cells were incubated with the test compound or complex for 72 h at 37 °C in a humidified 5% CO₂ incubator. The crystal violet staining technique as described was used to determine cytotoxic activity.⁵⁷ After 72 h, the test medium was removed, and the cells were washed three times with 300 µL of PBS. The cells were next fixed and stained for 10 min with 50 µL of crystal violet solution (0.03% crystal violet (w/v) in 20% methanol). The cells were then washed 6 times with 300 µL of distilled water, before adding 100 µL of lysis buffer to the cells for 20 min. The optical density of each well was measured at 620 nm, averaged over the set of six wells for each concentration, and the 50% cytotoxic concentration, or the concentration of test compound or complex that killed half of the cells was calculated using a non-linear least squares fit in KaleidaGraph (Synergy Software, Reading, PA, USA), and are expressed as the fitted $CC_{50} \pm SE(CC_{50})$, where the standard error of the parameter is derived from the parameter covariance matrix for the fit.

2.7. Viral infection assay

As described previously,⁵⁸ MDCK cells were seeded onto 12-mm glass coverslips at 2.4×10^4 cells/vial in 1 mL of DMEM with 5% FBS. The cells were incubated overnight at 37 °C in a humidified 5% CO₂ incubator. The culture was washed with serum-free medium to remove remaining FBS. SEM used in the miniplaque assay was selected for sustaining cell viability, allowing viral infection, and having minimal UV absorbance to allow easy determination of the complex stabilities. The EC_{50} for Amt was 3.4 ± 0.9 µM in SEM and 2.8 ± 0.3 µM in DMEM against the Amt-sensitive A/Victoria/03/75 H3N2.

Two to four replicates were done at each of five to six concentrations ranging from 1 to 50 µM, and four shell vials without any added test compound or complex served as controls. Stock

virus was thawed, treated with tosyl phenylalanyl chloromethyl ketone (TPCK) treated trypsin at 1 $\mu\text{g/mL}$, and then diluted with SEM to the appropriate dosage. The culture was inoculated with 100 μL of the solution containing activated virus, either A/Calif/07/09 H1N1, A/WS/33 H1N1, or A/ Victoria/03/75 H3N2, and incubated at 33 $^{\circ}\text{C}$ for 16 h. Coverslips were washed with phosphate-buffered saline (PBS), fixed with cold acetone (-80°C), and then removed from the shell vials. After air-drying for 30 min, the coverslips were stained with anti-IAV FITC-labeled monoclonal antibody (Light Diagnostics #5017, EMD Millipore – now Millipore Sigma, Billerica, MA) and incubated at 37 $^{\circ}\text{C}$ for 30 min in a humidified chamber. Excess antibody was washed off with PBS containing 0.05% Tween20, 0.5 mM MgCl and 3.1 mM sodium azide and distilled water. Miniplaques, defined as one or a few adjacent cells that were antibody-labeled (considering mitotic events and neighbor infection events as single miniplaques) were then counted with a fluorescent microscope. The 50%-effective concentrations (EC_{50}) were obtained by a non-linear least-squares fit using the Levenberg-Marquardt algorithm in KaleidaGraph and are expressed as the fitted $\text{EC}_{50} \pm \text{SE}(\text{EC}_{50})$, where the standard error of the parameter is derived from the parameter covariance matrix for the fit.

3. Results and discussion

3.1. Compound and complex synthesis and structure

Bromoacetic acid and bromoacetamide were added to Amt or cyclooctylamine to produce **1**, **3**, **5**, and **7** (Figure 2.2). Only a weak acetate base was required to promote the coordination of Cu^+ to **1** and **3**. A strong base, NaH was needed to deprotonate the amides of **5** and **7** and promote Cu^{2+} coordination.⁵⁹ Upon Cu^{2+} coordination to form **2**, **4**, **6**, and **8**, neutral complexes were formed due to the carboxylic acids and the amide nitrogens losing protons. Compounds **9**

and **10**, which were identical but without the scaffolds attached to the imino N, were formed from the amino diacetate or diacetamide.

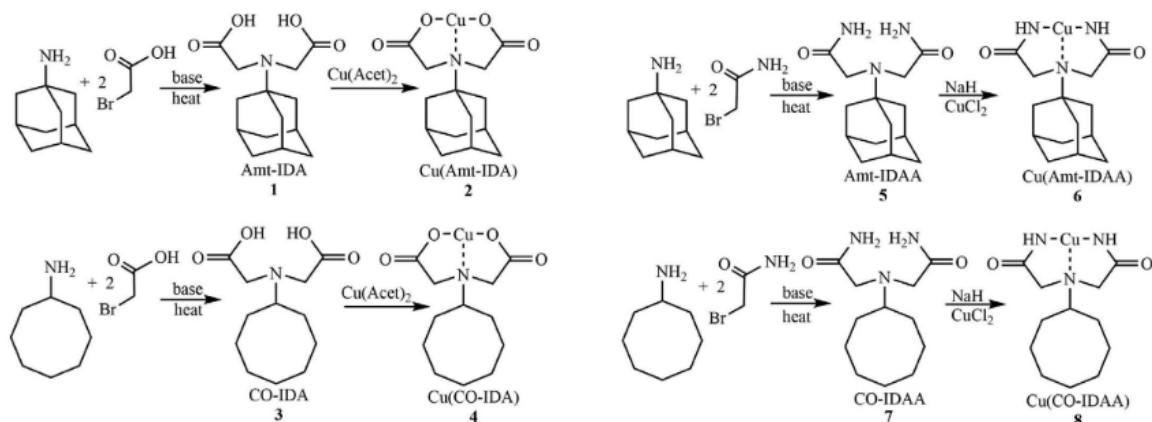


Figure 2.2. Synthetic procedures for compounds **1-8**.

Crystals of **2** were grown and X-ray analysis of the crystals showed ligand coordinating in a meridional arrangement around Cu^{2+} (Fig. 2.3). Water molecules occupy an equatorial position and one of the axial positions. The equatorial bonds are shorter and close to 2.0 Å, while the axial bond is longer (2.4 Å) due to Jahn-Teller distortion. The water molecules are labile and will exchange with stronger ligands, such as ligands containing nitrogen.⁶⁰ Except for a strong absorbance at around 200 nm, the Cu^{2+} -free compounds, **1**, **3**, **5**, and **7**, have very little

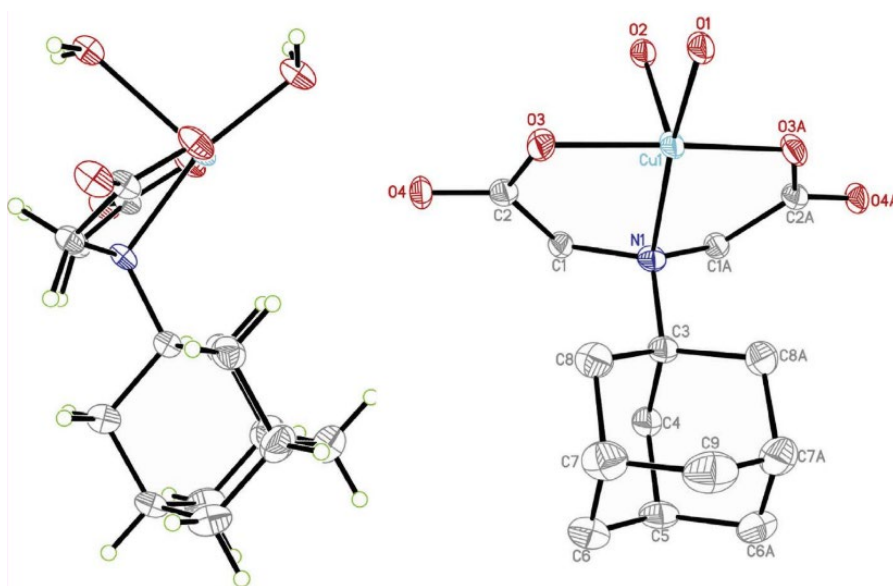


Figure 2.3. Crystal structure (side and face views) of **2**.

absorbance (data not shown). Once Cu^{2+} binding to the compounds occurs, a strong absorption band in the UV region at 250–280 nm is observed and absorption in the visible gives the complexes a blue coloration (see the legend of Fig. 2.5 for extinction coefficients).

3.2. Stability studies

UV absorption spectra of the complexes measured in water at therapy-like concentrations of 100 μM showed that **2**, **4** and **8** were stable in water for three days, while **6** showed moderate decomposition (Figure 2.4). The d-d transition produces absorption, enhanced by complexation, at visible wavelengths that could provide similar information. However, the extinction coefficient is ~ 100 -fold lower than for the absorbance in the UV, so for assays at the therapeutically relevant concentrations, we focused on UV measurements. Stability studies of the complexes in biological electrolyte solutions showed a good degree of stability for most of the complexes. In the SEM used for miniplaque assays, **2** and **4** were again stable for three days, but **8** showed some reduction in absorbance and **6** fully decomposed (Figure 2.5), whereas in Barth's all four spectra were stable.

In the Barth's solution used in the oocyte assays, as in SEM, **2** and **4** were stable (Figure 2.6). **6** and **8** showed changed UV-vis spectra with peak intensities being lower than they were in water. A reduction in absorption intensity implies a change in molar absorptivity, which would occur with the formation of a new complex. Most likely a new complex formed, potentially one with a buffer component bound to the copper in the complex. The absorbance bands, however, did not significantly decrease over the course of three days.

The metal complexes show good stability at pH ~ 7 . Judging from the UV spectra of 100 μM complexes in water titrated with HCl or NaOH, complexes **2** and **4** show stability over a pH range from 4 to 9. In contrast, the **6** and **8** are not stable at pH below 5 or above 13. IDAA has a

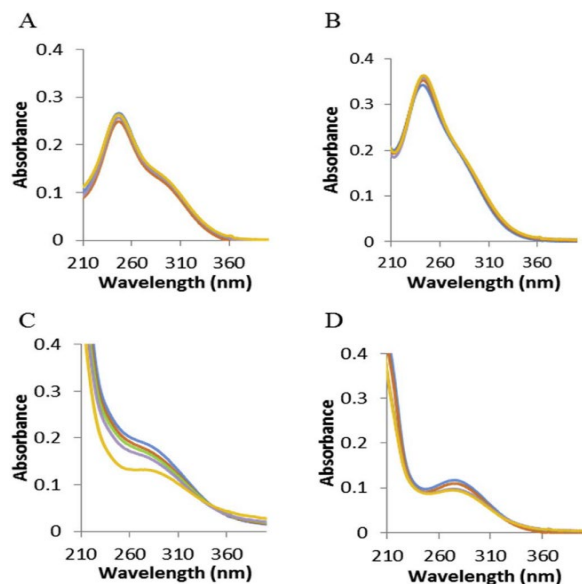


Figure 2.4. UV-Vis spectra of 100 μM solutions of (A) **2**, (B) **4**, (C) **6**, and (D) **8** in water. Spectra color: blue start, orange 4 h, green 12 h, purple 24 h, yellow 72 h.

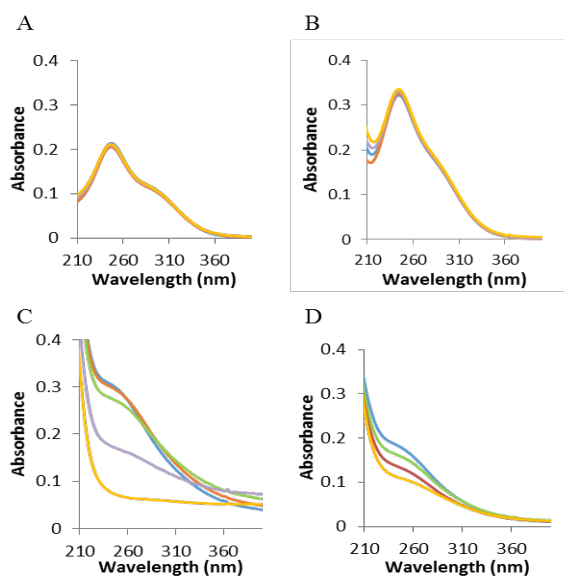


Figure 2.5. UV-Vis spectra of 100 μM solutions of (A) **2**, (B) **4**, (C) **6**, and (D) **8** in SEM. A spectrum of SEM was subtracted as background. Spectra color: blue start, orange 4 hrs, green 12 hrs, purple 24 hrs, yellow 72 hrs. Spectral bands in the UV region upon Cu^{2+} binding: 252 nm (5300 $\text{abs M}^{-1} \text{cm}^{-1}$) for **2**, 251 nm (3700 $\text{abs M}^{-1} \text{cm}^{-1}$) for **4**, 286 nm (1600 $\text{abs M}^{-1} \text{cm}^{-1}$) for **6**, and 285 nm (2800 $\text{abs M}^{-1} \text{cm}^{-1}$) for **8**. Along with the UV band, there is a new band in the visible region: 705 nm (220 $\text{abs M}^{-1} \text{cm}^{-1}$) for **2**, 717 nm (100 $\text{abs M}^{-1} \text{cm}^{-1}$) for **4**, 650 nm (200 $\text{abs M}^{-1} \text{cm}^{-1}$) for **6**, and 637 nm (170 $\text{abs M}^{-1} \text{cm}^{-1}$) for **8**. The UV absorption with its intermediate molar absorptivity is proposed to be due to a ligand-to-metal charge transfer (LMCT) and the peak in the visible is due to a copper-based d-d transition.

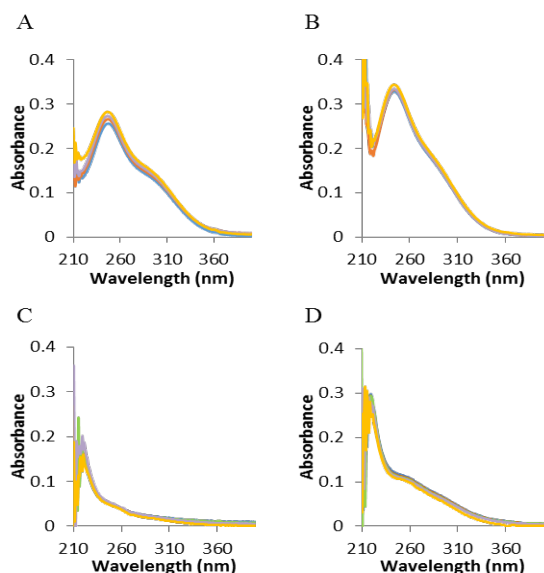


Figure 2.6. UV-Vis spectra of 100 μM solutions of (A) **2**, (B) **4**, (C) **6**, and (D) **8** in Barth's. A spectrum of Barth's solution was subtracted as background. Spectra color: blue start, orange 4 hrs, green 12 hrs, purple 24 hrs, yellow 72 hrs.

very high pK_a (around 17) and thus, because of the compound's strong affinity for protons, Cu^{2+} is out-competed by protons at moderate pH values. In comparison, the affinity of IDA for protons is much smaller, (with the pK_a expected to be near that of acetic acid, 4.8), so a lower pH is required for H^+ to out-compete Cu^{2+} for the binding site in the complex (data not shown).

3.3. 1H -NMR characterization

The decomplexation at low pH was used to characterize the complexes. Due to the paramagnetic nature of Cu^{2+} ions, no 1H -NMR signals or only broad peaks were visible when Cu^{2+} is bound to the compounds (Figure 2.7). However, after acidifying the complexes to $pH < 3$, the unbound ligand 1H -NMR signals are visible (Figure 2.8).

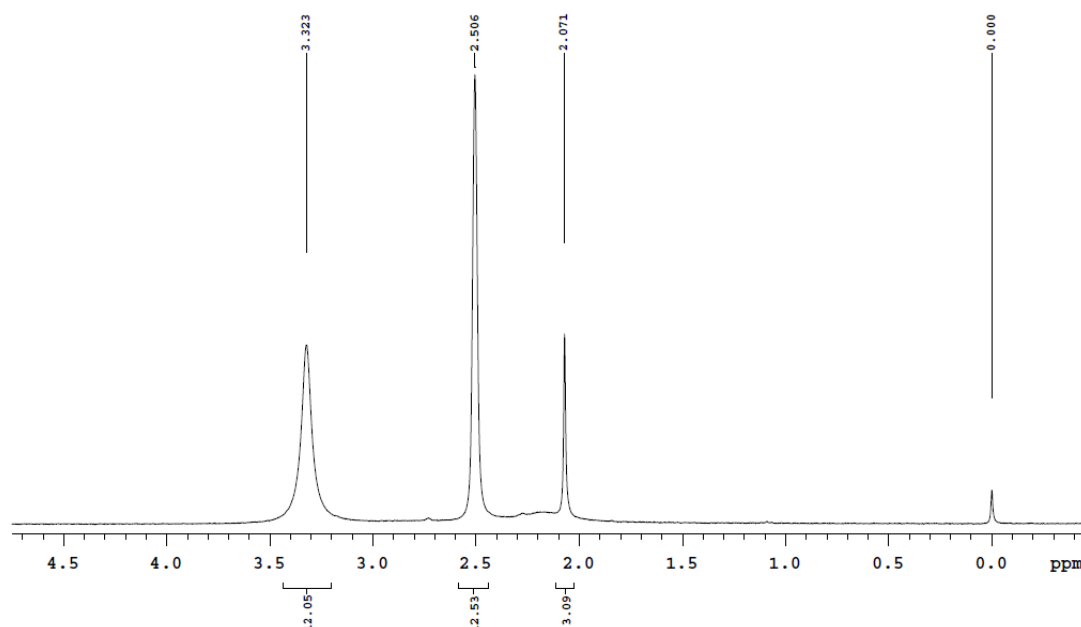


Figure 2.7. 1H -NMR (300 MHz) of **2** with an acetonitrile standard before acidification in $DMSO-d_6$. Peak assignments (ppm): 0.00 TMS, 2.07 $NCCH_3$, 2.51 DMSO, 3.32 H_2O .

3.4. Antiviral properties

Experimentally determined concentrations of CC_{50} , as well as EC_{50} against two standard strains of influenza A with the M2-S31N mutation, are given in Table 2.1. The only complex that

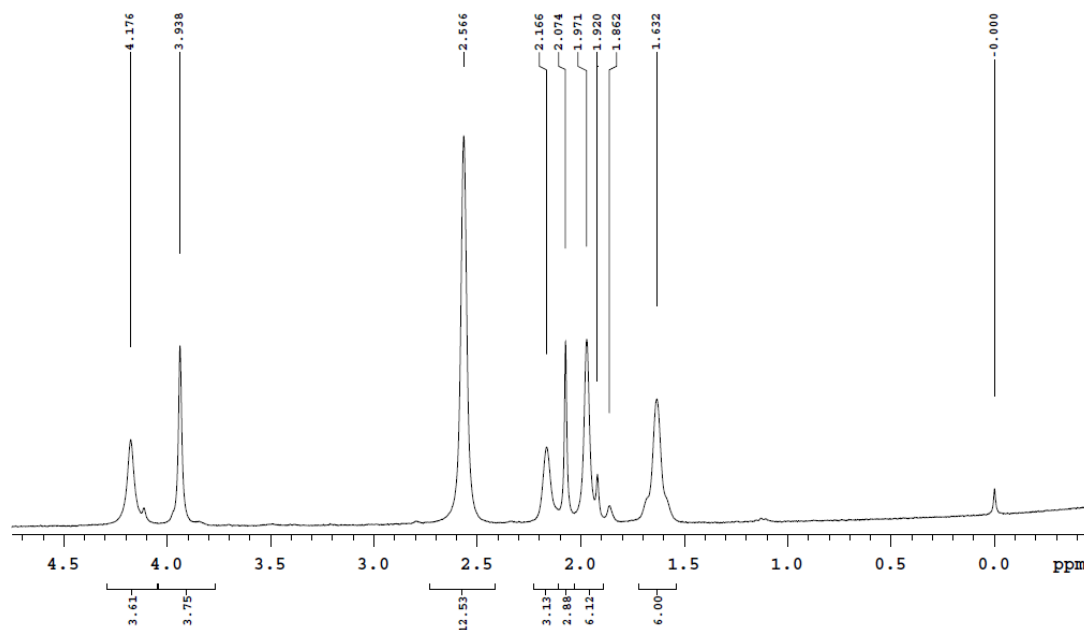


Figure 2.8. ^1H -NMR (300 MHz) of **2** with an acetonitrile standard after acidification with trifluoroacetic acid in DMSO-d_6 . Peak assignments (ppm): 0.00 TMS, 1.63 adamantane CH_2 , 1.97 adamantane CH_2 , 2.07 NCCH_3 , 2.17 adamantane CH , 2.57 DMSO, 3.94 H_2O , 4.18 IDA CH_2 .

Table 2.1. Cytotoxicity and efficacy data for CuCl_2 , **2**, **4**, **6**, **8**, **9**, and **10**.

Compound	CC_{50} (μM , S31N)	EC_{50} (μM , A/CA/07/09 H1N1 M2-S31N)	EC_{50} (μM , A/WS/33 H1N1 M2-S31N)
CuCl_2	19 ± 6	3.8 ± 0.9	4.3 ± 1.0
2	64 ± 7	6.9 ± 1.2	2.4 ± 0.3
4	147 ± 38	0.7 ± 0.1	2.1 ± 0.7
6	52 ± 5	4.9 ± 0.8	4.1 ± 2.4
8	180 ± 15	11.6 ± 1.1	2.3 ± 0.2
9	115 ± 9	8.2 ± 2.0	4.7 ± 1.1
10	64 ± 6	4.4 ± 0.6	7.2 ± 5.3

was more effective than the free copper in the 2009 pandemic strain (A/CA/07/09 H1N1 M2-S31N) was **4**. That was also the only complex that gave a CC_{50} over 100 μM and a sub- μM EC_{50} against either strain. All complexes except **9** and **10** exhibited lower EC_{50} s than CuCl_2 , highlighting the importance of the Amt and CO scaffolds on the complexes. Curiously, **8**

performed well with the highest CC_{50} of all the complexes and the second lowest EC_{50} against the WS strain. However, the dissociation shown in the UV-Vis stability studies made meaningful observations difficult to derive from direct comparisons to other complexes. Notably, the copper-free ligands performed similarly to amantadine in both the M2-S31N mutant and the M2-S31 WT virus (data not shown).

Experimentally determined data for M2 channel block for $CuCl_2$, Amt, and complexes **1-10** are given in Table 2.2 as the average and standard deviation from 3 assays. The TEVC trace of $CuCl_2$ (Figure 2.9A) was the standard trace against which the other traces were compared, as it

Table 2.2. M2 block of $CuCl_2$, Amt, **2, 3, 4, 6, 8, 9**, and **10**. All data represent the average of 3 replicates.

Compound	% Block Fast (S31N)	% Block Total (S31N)	% Block Recovered (S31N)	% Block (H37A)	% Block Recovered (H37A)
$CuCl_2$	18 ± 1.4	95 ± 2.8	None	19.8 ± 0.3	14.9 ± 0.2
2	10.5 ± 2.1	91.5 ± 7.8	9.0 ± 1.4	<i>N.T.</i>	<i>N.T.</i>
4	11.5 ± 0.7	90.5 ± 2.1	1.2 ± 0.3	12.0 ± 2.8	6.0 ± 1.4
6	18.5 ± 2.1	91.5 ± 4.2	7.5 ± 0.7	<i>N.T.</i>	<i>N.T.</i>
8	25 ± 2.8	66.5 ± 5.0	24 ± 0.2	26 ± 10.9	24.6 ± 14.1
9	5.9 ± 0.1	17.9 ± 2.9	1.7 ± 1.9	<i>N.T.</i>	<i>N.T.</i>
10	33.5 ± 0.7	68.0 ± 2.8	22 ± 1.4	<i>N.T.</i>	<i>N.T.</i>
Amantadine*	30.5 ± 1.3 (93.6 ± 2.6)	None (None)	29.1 ± 1.4 (None)	<i>N.T.</i>	<i>N.T.</i>
1	6.5 ± 1.5	None	None	<i>N.T.</i>	<i>N.T.</i>
3	42.8 ± 0.6	None	33.4 ± 1.7	6.8 ± 0.4	4.5 ± 0.7
5	9.6 ± 8.3	None	5.6 ± 3.7	<i>N.T.</i>	<i>N.T.</i>
7	12.5 ± 2.5	None	6.8 ± 0.4	<i>N.T.</i>	<i>N.T.</i>

*Data in parentheses were tested against M2-S31 WT. N.T. = not tested.

showed a steady increase in current block with no current recovery after a compound-free rinse solution was introduced. Complex **4** again stood out with high block ($90.5 \pm 2.1\%$) and only a slight ($1.2 \pm 0.3\%$) recovery, and its trace (Figure 2.9B) clearly shows a fast-phase block as the initial, almost vertical increase, and a slow-phase block as the creeping upward trend over time. Compound **3**, by comparison, showed the highest fast-phase block ($42.8 \pm 0.6\%$) but no slow-phase block, and most of its block was recovered ($33.4 \pm 1.7\%$) with the introduction of the rinse solution. This strong recovery created a characteristic “plateau” curve (Figure 2.9C) also exhibited by Amt against both M2-S31 WT and M2-S31N, the other copper-free ligands **1**, **5**, and **7** against M2-S31N, and CuCl₂ and the metal complexes **4** and **8** against M2 H37A. Despite its strong CC₅₀ and EC₅₀ against the WS virus, **8** blocked the M2-S31N channel poorly relative to the other metal complexes.

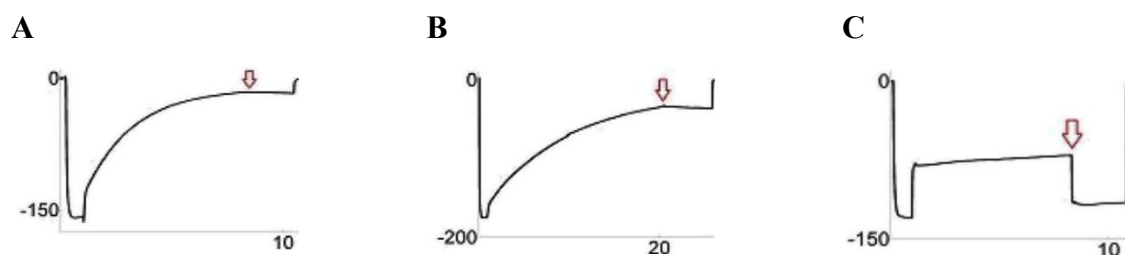


Figure 2.9. TEVC traces in Barth's solution of (A) CuCl₂, (B) **4**, and (C) **3**. Upward trend represents channel block. The valley at time near 0 represents 0% block, 0 represents 100% block, beginning of upward trend represents introduction of compound solution, red arrow indicates when compound solution was replaced with compound-free rinse solution, and drop after red arrow represents current recovery.

Comparison of the performance of CuCl₂ and the copper complexes against S31N and H37A shows that, in every case, their block against H37A had no slow phase increase and very closely mirrored their fast-phase block against S31N. These observations strongly suggest that the presence of any blocking compound was responsible for the fast-phase block and that the presence of both histidine and copper was responsible for the slow-phase block and the much lower current recovery relative to their respective ligands. Also noteworthy is the poor

performance of **9** and **10**, providing further evidence that the presence of the Amt or CO scaffold is important to M2-S31N inhibition.

4. Conclusions

We confirmed that Cu^{2+} blocks the native M2 channel and also found that it blocks M2-S31N in voltage-clamped transfected *Xenopus* oocytes. The washout shows that copper binds tightly in both M2 constructs. When Cu^{2+} is complexed via IDA or IDAA with or without derivatives of known M2 blockers, Amt or cyclooctylamine, the complexes block M2 channels comparably to aquated Cu^{2+} . When the Cu^{2+} is removed from the complex, the tight block is eliminated, which suggests Cu^{2+} in the complex is adhering to the M2 channels. When the histidines are mutated to alanines (H37A), the slow block is also eliminated, indicating that the copper complexes bind to the histidines of the M2 channels during the slow phase. The copper complexes significantly reduce, with low cytotoxicity, infection of MDCK cells with three IAV strains, two Amt-insensitive and one Amt-sensitive, and have EC_{50} s in MDCK cell culture for the three strains of IAV of 0.7–11.6 μM . Complexation reduces the cytotoxicity of Cu^{2+} approximately 10-fold.

Although the adamantyl and cyclooctyl moieties don't affect the antiviral efficacy on the long time scale, it is clear that they enhance M2 blocking on the short time scale of oocyte experiments (**2**, **4** > **9** and **6**, **8** > **10**). One complex in particular, **4**, is potent at sub-micromolar concentrations against A/Calif/07/2009 H1N1, has a low cytotoxicity (average therapeutic index 67.8), and withstands decomposition in phosphate, sulfate, and nitrate containing buffers on the timescale of infection and experiments. Considering the human dietary tolerance for copper and the measured EC_{50} s, we estimate that these complexes could be useful as novel treatments against multiple strains of IAV. They could be delivered either by inhalant, orally in acid-

resistant encapsulation, or intravenously. Resistance testing and animal testing are needed to further explore these possibilities.

Acknowledgements

Mackenzie Hart, McKay Jensen, and James Clark provided technical assistance. The work was supported by a grant from National Institutes of Health (AI 23007), a BYU College High Impact Research Proposal award, and BYU Mentoring Environment Grants. The funding sources had no involvement in design, execution, or communication of the report.

References

1. Martin, K.; Helenius, A. *Cell* **1991**, *67*, 117–130.
2. Sugrue, R. J.; Bahadur, G.; Zambon, M. C.; Hall-Smith, M.; Douglas, A. R.; Hay, A. J. *EMBO J.* **1990**, *9*, 3469–3476.
3. Davies, W. L.; Grunert, R. R.; Haff, R. F.; McGahen, J. W.; Neumayer, E. M.; Paulshock, M.; Watts, J. C.; Wood, T. R.; Hermann, E. C.; Hoffmann, C. E. *Science* **1964**, *144*, 862–863.
4. Wang, C.; Takeuchi, K.; Pinto, L. H.; Lamb, R. A. *J. Virol.* **1993**, *67*, 5585–5594.
5. Chizhmakov, I. V.; Geraghty, F. M.; Ogden, D. C.; Hayhurst, A.; Antoniou, M.; Hay, A. J. *J. Physiol.* **1996**, *494* (Pt 2), 329–336.
6. Krylov, V. F.; Alekseeva, A. A.; Lyarskaia, T. Y.; Polyakova, T. G.; Kupryashina, L. M.; Berlyand, M. L.; Furman, M. A. *Vopr. Virusol.* **1976**, *2*, 186–191.
7. Hay, A. J.; Wolstenholme, A. J.; Skehel, J. J.; Smith, M. H. *EMBO J.* **1985**, *4*, 3021–3024.
8. Pinto, L. H.; Holsinger, L. J.; Lamb, R. A. *Cell* **1992**, *69*, 517–528.
9. Hata, M.; Tsuzuki, M.; Goto, Y.; Kumagai, N.; Harada, M.; Hashimoto, M.; Tanaka, S.; Sakae, K.; Kimura, T.; Minagawa, H.; Miyazaki, Y. *Jpn. J. Infect. Dis.* **2007**, *60*, 202–204.
10. Krumbholz, A.; Schmidtke, M.; Bergmann, S.; Motzke, S.; Bauer, K.; Stech, J.; Dürrwald, R.; Wutzler, P.; Zell, R. *J. General Virol.* **2009**, *90*, 900–908.
11. Wu, Y.; Canturk, B.; Jo, H.; Ma, C.; Gianti, E.; Klein, M. L.; Pinto, L. H.; Lamb, R. A.; Fiorin, G.; Wang, J.; DeGrado, W. F. *J. Am. Chem. Soc.* **2014**, *136*, 17987–17995.
12. Zhao, X.; Jie, Y.; Rosenberg, M. R.; Wan, J.; Zeng, S.; Cui, W.; Xiao, Y.; Li, Z.; Tu, Z.; Casarotto, M. G.; Hu, W. *Antivir. Res.* **2012**, *96*, 91–99.
13. Balannik, V.; Wang, J.; Ohigashi, Y.; Jing, X.; Magavern, E.; Lamb, R. A.; Degrado, W. F.; Pinto, L. H. *Biochemistry* **2009**, *48*, 11872–11882.
14. Wang, J.; Ma, C.; Jo, H.; Canturk, B.; Fiorin, G.; Pinto, L. H.; Lamb, R. A.; Klein, M. L.; Degrado, W. F. *J. Med. Chem.* **2013**, *56*, 2804–2812.
15. Venkataraman, P.; Lamb, R. A.; Pinto, L. H. *J. Biol. Chem.* **2005**, *280*, 21463–21472.

16. Wang, C.; Lamb, R. A.; Pinto, L. H. *Biophys. J.* **1995**, *69*, 1363–1371.
17. Gandhi, C. S.; Shuck, K.; Lear, J. D.; Dieckmann, G. R.; DeGrado, W. F., Lamb, R.A., Pinto, L.H. *J. Biol. Chem.* **1999**, *274*, 5474–5482.
18. Su, Y.; Hu, F.; Hong, M. *J. Am. Chem. Soc.* **2012**, *134*, 8693–8702.
19. Blumenstyck, G. *Chron. High. Educ.* **1999**, *12*, A39–A40.
20. Barnes, K. R.; Lippard, S. J. *Met. Ions Biol. Syst.* **2004**, *42*, 143–177.
21. Bloemink, M. J.; Reedijk, J. *Met. Ions Biol. Syst.* **1996**, *32*, 641–685.
22. Alderden, R. A.; Hall, M. D.; Hambley, T. W. *J. Chem. Educ.* **2006**, *83*, 728–734.
23. Boulikas, T.; Vougiouka, M. *Oncology Reports* **2004**, *11*, 559–595.
24. Dabrowiak, J. C. *Metals in Medicine*; Wiley: United Kingdom, 2009; 109-141, 149-182.
25. Messori, L; Giordana, M. *Met. Ions Biol. Syst.* **2004**, *41*, 279–304.
26. Forestier, J. *Lancet* **1934**, *2*, 646–648.
27. Zhang, C. X.; Lippard, S. J. *Curr. Opin. Chem. Biol.* **2003**, *7*, 481–489.
28. Thompson, K. H.; McNeill, J. H.; Orvig, C. *Chem. Rev.* **1999**, *99*, 2561–2571.
29. Choi, W. T.; Tian, S. M.; Dong, C. Z.; Kumar, S.; Liu, D. X.; Madani, N.; An, J.; Sodroski, J. G.; Huang, Z. W. *J. Virol.* **2005**, *79*, 15398–15404.
30. Bush, A. I. *J. Alzheimers Dis.* **2008**, *15*, 223–240.
31. Jabłńska-Kaszewska, I.; Dabrowska, E.; Drobinska-Jurowiecka, A.; Falkiewicz, B. *Med. Sci. Monit.* **2003**, *9* (Suppl 3), 5–8.
32. Hoogenraad, T. U. *Brain Dev.* **2006**, *28*, 141–146.
33. Brewer, G. J. *Expert Opin. Invest. Drugs* **2009**, *18*, 89–97.
34. Ferrada, E.; Arancibia, V.; Loeb, B.; Norambuena, E. *NeuroToxicol.* **2007**, *28*, 445–449.
35. Atwood, C. S.; Scarpa, R. C.; Huang, X. D.; Moir, R. D.; Jones, W. D.; Fairlie, D. P.; Tanzi, R. E.; Bush, A. I. *J. Neurochem.* **2000**, *75*, 1219–1233.
36. Treiber, C.; Simons, A.; Strauss, M.; Hafner, M.; Cappai, R.; Bayer, T. A.; Multhaup, G. *J. Biol. Chem.* **2004**, *279*, 51958–51964.
37. Sarkar, B. *Chem. Rev.* **1999**, *99*, 2535–2544.
38. Alizadeh, R.; Yousuf, I.; Afzal, M.; Srivastav, S.; Srikrishna, S.; Arjmand, F. *J. Photochem. Photobiol. B, Biol.* **2015**, *143*, 61–73.
39. Anjomshoa, M.; Torkzadeh-Mahani, M.; Dashtrazmi, E.; Adeli-Sardou, M. *J. Fluoresc.* **2016**, *26*, 545–558.
40. Hajrezaie, M.; Paydar, M.; Moghadamtousi, S. Z.; Hassandarvish, P.; Gwaram, N. S.; Zahedifard, M.; Rouhollahi, E.; Karimian, H.; Looi, C. Y.; Ali, H. M.; Abdul Majid, N.; Abdulla, M. A. *Sci. World J.* **2014**, 540463.
41. Iakovidis, I.; Delimaris, I.; Piperakis, S. M. *Mol. Biol. Int.* **2011**, 594529.
42. Tabassum, S.; Al-Asbahy, W. M.; Afzal, M.; Arjmand, F.; Khan, R. H. *Mol. Biosyst.* **2012**, *8*, 2424–2433.
43. Tabassum, S.; Asim, A.; Arjmand, F.; Afzal, M.; Bagchi, V. *Eur. J. Med. Chem.* **2012**, *58*, 308–316.

44. Tabassum, S.; Amir, S.; Arjmand, F.; Pettinari, C.; Marchetti, F.; Masciocchi, N.; Lupidi, G.; Pettinari, R. *Eur. J. Med. Chem.* **2013**, *60*, 216–232.
45. Tabassum, S.; Zaki, M.; Afzal, M.; Arjmand, F. *Eur. J. Med. Chem.* **2014**, *74*, 509–523.
46. Mao, Z. W.; Liehr, G.; van Eldik, R. *J. Am. Chem. Soc.* **2000**, *122*, 4839–4840.
47. Nevitt, T.; Öhrvik, H.; Thiele, D. *Biochem. Biophys. Acta* **2012**, *1823*, 1580–1593.
48. Xiao, Z.; Loughlin, F.; George, G. N.; Howlett, G. J.; Wedd, A. G. *J. Am. Chem. Soc.* **2004**, *126*, 3081–3090.
49. Bull, R.; Aschner, M.; Brewer, G.; Harris, E.; Keen, C.; Kelsey, K.; Sunderman, F. W. J.; Tsuji, J.; Zeise, L.; Maczka, C. A.; Catlin, M. C.; Crossgrove, R. E.; Estep, J. L.; Holliday, L. T.; Karalic-Loncarevic, M. *Copper in Drinking Water*; National Academies Press: Washington, D.C., 2000.
50. Li, F.; Ma, C.; DeGrado, W. F.; Wang, J. *J. Med. Chem.* **2016**, *59*, 1207–1216.
51. Wang, J.; Li, F.; Ma, C. *Biopolymers* **2015**, *104*, 291–309.
52. Durrant, M. G.; Eggett D. L.; Busath D. D. *BMC Genet.* **2015**, *16* (Suppl. 2), S3.
53. Pinto, C. A.; Haff, R. F. *Antimicrob. Agents* **1968**, *Ch. 8*, 201–206.
54. Lin, T. I.; Heider, H.; Schroeder, C. *J. Gen. Virol.* **1997**, *78*, 767–774.
55. Fernández-Piñar, R.; Sánchez de Medina-Revilla, C.; Domínguez-Martín, A.; Pilar Brandi-Blanco, M.; Choquesillo-Lazarte, D.; María González-Pérez, J.; Niclós-Gutiérrez, J. Z. *Anorg. Allg. Chem.* **2007**, *633*, 2658–2666.
56. Roman-Alpiste, M. J.; Martin-Ramos, J. D.; Castineiras-Campos, A.; Bugella-Altamirano, E.; Sicilia-Zafra, A. G.; Gonzalez-Perez, J. M.; Niclos-Gutierrez, J. *Polyhedron* **1999**, *18*, 3341–3351.
57. Schmidtke, M.; Schnittler, U.; Jahn, B.; Dahse, H.; Stelzner, A. *J. Virol. Methods* **2001**, *95*, 133–143.
58. Kolocouris, A.; Tzitzoglaki, C.; Johnson, F. B.; Zell, R.; Wright, A. K.; Cross, T. A.; Tietjen, I.; Fedida, D.; Busath, D. D. *J. Med. Chem.* **2014**, *57*, 4629–4639.
59. Rowland, J.; Thornton, M.; Olmstead, M.; Mascharak, P. *Inorg. Chem.* **2001**, *40*, 1069–1073.
60. Conry, R. R. Copper: Inorganic & Coordination Chemistry, In *Encyclopedia of Inorganic Chemistry*, 2nd ed.; King, R.B., Ed.; King, R.B., Ed.; John Wiley & Sons, Inc.: Wiley Online Library, 2006.

CHAPTER 3

Crystal Structures and Influenza A Inhibition of Divalent Polyamine Copper Complexes

Abstract

Influenza A (IVA) continues to pose a growing global threat even as current medications are becoming less effective. One of the main avenues of research into new anti-IVA drugs is its M2 proton channel, especially the mutant M2-S31N (M2A). Building on the foundation of past copper-containing M2A blockers targeting the M2A-H37 cluster, a series of copper complexes featuring polyaza or polyamine chelators was developed. The effects of complex charge and stability on ability to block M2A are examined. Complex **3**, and its ligand **3L**, were novelly synthesized and all complexes were fully characterized. The crystal structure of **3**, as well as that of **1** and **2**, were solved and are reported. The inverted-twin structure of **1**, the tight packing and high stability of **2**, and the alternating hydrophobic and hydrophilic bands of **3** are discussed. Though these complexes showed M2A inhibition inferior to previous anti-M2A copper complexes, these complexes are useful to guide the direction of metal-containing M2A blockers.

1. Introduction

The influenza A virus (IVA) continues to be a global problem, especially for the very young and the elderly.¹ Amantadine (Amt), or adamantylamine, was an effective anti-IVA drug that targeted the virus's Matrix 2 proton channel V27 and S31 sites, until it was made obsolete in the early 2000s when the IVA Matrix 2-S31N mutation (M2A) became nearly ubiquitous across all IVA strains.² Amt worked by blocking the influx of protons through M2-WT to disable the virus, employing both hydrogen bonding through its amine and hydrophobic interactions through the hydrocarbon ring, thereby preventing the activation of the viral RNA transfer process.³ For the

past two decades, research has been ongoing to discover replacement drugs to fight IVA, much of which has centered around replacing Amt with effective small organic ligand M2A-S31N inhibitors (see Chapter 1).

Our team has focused on developing metal chelates using N-substitution of amantadine or similar cyclic amines, adding “arms” that could bind the metal center while leaving it free enough to bind M2A at its absolutely conserved H37 site. Because copper has been shown to dramatically outperform other first-row transition metals in M2A-H37 binding strength and irreversibility, we chose copper as our metal of interest.^{4,5} Because of copper’s toxicity, however, decomplexation and cytotoxicity were a primary concern in our research.⁶

Our previous work comprised the formation and *in vitro* testing of neutral trichelate copper complexes as novel anti-IVA drug candidates (Gordon *et al.*, 2017). That line of research found that, while copper complexes of amantadine iminodiacetate (Amt-IDA), amantadine iminodiacetamide (Amt-IDAA), cyclooctyl iminodiacetate (CO-IDA), and cyclooctyl aminodiacetamide (CO-IDAA) (Figure 3.1) were effective at blocking the M2A-S31N channel at low-micromolar concentrations, the Cu(Amt-IDAA) and Cu(CO-IDAA) complexes lacked the high stability possessed by the Cu(Amt-IDA) and Cu(CO-IDA) complexes when dissolved in water. Further, we found that the cyclooctyl scaffold was as effective as the Amt scaffold, though its lack of a rigid structure made characterizing it somewhat more difficult, especially by single crystal X-ray diffraction (SC-XRD).

In this work, we chose to develop polyamine complexes of Cu²⁺ charge that would be dicationic in aqueous solution. The amines would also be stronger ligands than the previously used carboxylic acids and increase the stability of the copper complexes. We chelated copper with 1,4,7,10-tetraazacyclododecane (cyclen), 1,3,7-triazacyclononane (TACN), and N,N’-bis(2-

pyridylmethyl)amantadine (Figure 3.1). Using cyclen with various copper salts to determine a good counter anion, we decided on sulfate, it being more biologically benign than perchlorate and having superior lattice properties to chloride in the solid state.

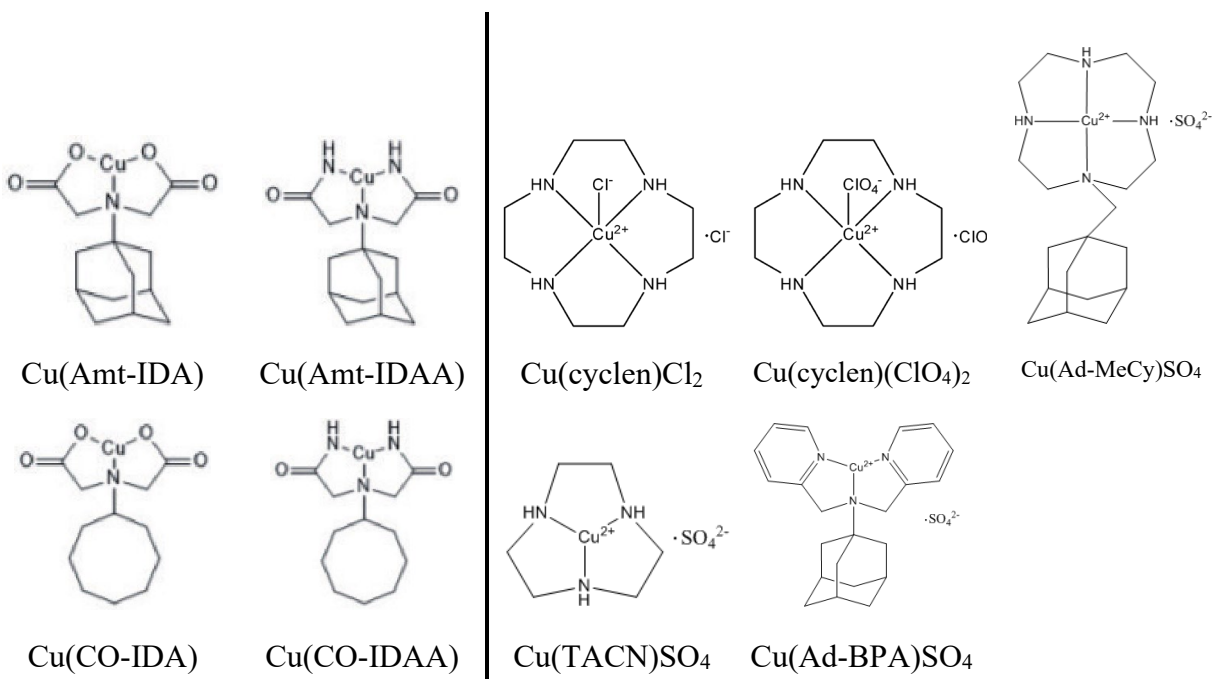


Figure 3.1. Structures of neutral and divalent copper complexes. Structures detail (A) Previously reported work with neutral complexes, and (B) This work with divalent complexes.

Cyclen has a long history as a polyaza macrocycle for metal complexation, and along with its cousin, cyclam, acts as a powerful 1:1 metal chelator, particularly for copper.⁸ For instance, Kim and coworkers showed that cyclen could be embedded in a larger macrocycle, and they further demonstrated that copper and zinc behaved very similarly when complexed by cyclen in that system.⁹ Additionally, our group showed that a zinc-cyclen-resorcinarene structure can act as an effective stationary phase for anion separation,¹⁰ while the uncomplexed cyclen-resorcinarene showed limited effect in the same application.¹¹ Research is still ongoing in cyclen metal complexes, as Tsebrikova and coworkers recently reported on the synthesis and characterization of the first octacoordinate cyclen complexes incorporating divalent zinc and cobalt.¹²

The rigid structure of metal-cyclen complexes makes them ideal for crystallography, especially when coupled with a hydrogen bonding-active anion such as perchlorate or sulfate. One point of interest in metal-cyclen crystal structures includes the complexes' puckered geometry, usually mentioned as the M-(plane N₄) distance.¹² The packing structure can also yield important information; the rapid decay of some complexes can be attributed to their loose packing and easy escape of solvent molecules.¹² In the case of copper-cyclen complexes, Jahn-Teller distortion in the Cu(II) makes the distance of the axial bond interesting as well.¹³

A great number of crystal structures have been reported for metal-cyclen complexes. Indeed, over 200 structures were found for copper-cyclen and zinc-cyclen complexes alone. Most of these are for substituted cyclen rings, however. One study was found that reported structures for two different hydration states of Cu(cyclen)SO₄,¹³ and another for Cu(cyclen)(NO₃)₂.¹⁴ However, no structures were found for the unsubstituted complexes of dichloro copper-cyclen (**1**) or diperchlorato copper-cyclen (**2**). These structures will be reported here.

Additionally, while extensive work has been performed with substituted cyclens, and there are many known structures with amantadine groups bound to transition metals, no crystal structure was found in the Cambridge Crystallographic Data Centre (CCDC) database with an adamantane substituent on a cyclen or cyclam ring. Some applications could benefit from the conjunction of the site specificity and increased lipophilicity of adamantane with a strongly bound transition metal, such as preferential targeting of M2A. Additionally, adamantane's ability to enhance other pharmacological properties, such as pharmacokinetics, stability and distribution in blood plasma, channel blocking and fitting for other cavities, and transport through lipids, could particularly aid research in these fields.¹⁵ For example, an adamantane-substituted metal-cyclen complex could target drug delivery for protein inhibition as the adamantane could direct

the complex to a particular binding site while the metal binds a nearby residue through its open axial site.

In the work detailed herein, we explored binding copper to neutral polyamine chelates, resulting in divalent complexes (Figure 3.1, B). Unlike our previous work, we synthesized tetrachelate complexes in addition to trichelates and used nitrogens as the chelating atoms to create stronger metal-ligand bonds in an attempt to increase stability. We explored the heterocyclic chelators cyclen (**1-3**) and TACN (**4**) as well as an adamantyl derivative of dipicolylamine (**5**). The novel ligand with cyclen bonded to adamantyl was synthesized and bound to copper (**3**). We also solved crystal structures of **1-3**, which are unknown in the literature and will be discussed here. The M2A blocking results for the complexes will also be given.

2. Experimental

2.1. Synthesis

2.1.1. General considerations

All reagents were of analytical grade and were purchased commercially and used without further purification. Cyclen (**1L**, **2L**) was obtained commercially and used as received. ^1H and ^{13}C -NMR spectra were recorded on a Bruker 500 MHz multinuclear FT-NMR spectrometer. Proton chemical shifts were reported in parts per million (δ) with reference to tetramethylsilane (TMS, δ 0.0 ppm) or their respective solvent peaks. Mass measurements were done on an Agilent model G1969A LC/MSD TOF mass spectrometer.

CAUTION! While no problems were experienced with the salts in this study, perchlorate salts of metal complexes and organic ligands are potentially explosive and should be handled with care.

2.1.2. Synthesis of Cu(Cyclen)Cl₂ (**1**)

This procedure was modified from literature.^{16,17} Copper chloride dihydrate (0.68 g, 4.0 mmol) was dissolved in 15 mL of methanol. Separately, cyclen (0.69 g, 4.0 mmol) was dissolved in 15 mL of methanol. The copper solution was added to the cyclen solution, and a color change to dark blue occurred immediately. The mixture was refluxed for 30 minutes, and the volume of the resulting solution was reduced by half. Diethyl ether was added, causing blue and green crystals of **2** to precipitate. More diethyl ether was added, and blue crystals precipitated. The crystals of **1** were collected in 89% yield (1.0886 g).

2.1.3. Synthesis of Cu(Cyclen)(ClO₄)₂ (**2**)

This complex was synthesized according to a procedure from the literature in 88.4% yield.¹⁶

2.1.4. Synthesis of N-((adamant-1-yl)methyl)-cyclen (**3L**)

The reaction was performed under dry conditions under a nitrogen atmosphere. Cyclen (1.3782 g, 8.0 mmol) was dissolved in 60 mL acetonitrile in a pressure vessel, and triethylamine (2.80 mL, 20.1 mmol) was added to this solution while stirring. Separately, 1-(bromomethyl)-adamantane (0.9181 g, 4.0 mmol) was dissolved in 30 mL acetonitrile, and this solution was then slowly added to the cyclen solution. The pressure vessel was sealed, and the reaction was refluxed at 150 °C for 6 days. The resulting cloudy solution was filtered under ambient atmosphere and rinsed with acetonitrile at 0 °C, and the resulting white residue was dried under vacuum to give a 44% yield (0.5669 g) of product. ¹H-NMR (500 MHz, CDCl₃): δ (ppm) 2.84 (s, 2H, NH), 2.80 (s, 4H, cyclen CH₂), 2.65 (s, 4H, cyclen CH₂), 2.58 (s, 4H, cyclen CH₂), 2.52 (s, 4H, cyclen CH₂), 2.06 (s, 2H, bridging CH₂), 1.97 (s, 3H, adamantane CH), 1.65 (m, 6H, adamantane CH₂), 1.56 (d, 6H, adamantane CH₂), 1.06 (s, 1H, NH). ¹H-NMR (500 MHz, CDCl₃ + 2 drops CH₃OH): δ (ppm) 2.78 (s, 4H, cyclen CH₂), 2.62 (s, 4H, cyclen CH₂), 2.55 (bs, 8H,

cyclen CH₂), 2.08 (s, 2H, bridging CH₂), 1.98 (s, 3H, adamantane CH), 1.68 (m, 6H, adamantane CH₂), 1.55 (d, 6H, adamantane CH₂). HRMS (ESI) m/z: calculated for [C₁₉H₃₆N₄ + H⁺] 321.3013; Found: 321.3012.

2.1.5. Synthesis of [Cu(N-((adamant-1-yl)methyl)-cyclen)]SO₄ (**3**)

CuSO₄·5H₂O (0.2500 g, 1.0 mmol) was dissolved in 50 mL of water and poured over solid N-((adamant-1-yl)methyl)-cyclen (0.3201 g, 1.0 mmol), and the solution immediately turned dark blue. The solution was refluxed for 48 hours, and the solvent was removed under vacuum. The resulting blue solid was recrystallized via evaporation of methanol. This mixture was filtered and the solid rinsed with acetone, which caused more solid to precipitate in the filtrate. The filtrate was filtered again, and both solids were collected as an indigo powder in 44% yield (0.2093 g). ¹H-NMR (500 MHz, DMSO-d₆): no compound peaks. ¹H-NMR (500 MHz, DMSO-d₆ + 30 μL DCl [35% w/w in D₂O]): δ (ppm) 3.44 (bs, 12H, cyclen non-α-CH₂), 3.27 (bs, 4H, cyclen α-CH₂), 3.13 (bs, 2H, bridging CH₂), 2.03 (bs, 3H, adamantane CH), 1.89 (bs, 6H, adamantane CH₂), 1.61 (bs, 6H, adamantane CH₂). HRMS (ESI) m/z: calculated for [Cu(C₁₉H₃₆N₄) - H⁺] 382.2152, [Cu(C₁₉H₃₆N₄) + CHO₂⁻] 428.2207; found: 382.2151, 428.2210.

2.1.6. Synthesis of TACN (**4L**)

TACN was synthesized as previously described¹⁸ and refrigerated between uses in a sealed flask evacuated with nitrogen.

2.1.7. Synthesis of [Cu(TACN)]SO₄ (**4**)

This procedure was identical to the synthesis of **2** using TACN instead of cyclen and the sulfate salt of copper instead of perchlorate.

2.1.8. Synthesis of N,N'-bis(2-pyridylmethyl)amantadine (**5L**)

This compound was synthesized according to a procedure from the literature in 38.1% yield.¹⁹

2.1.9. Synthesis of [Cu(N,N'-bis(2-pyridylmethyl)amantadine)]SO₄ (**5**)

The synthesis of this complex was modified from a literature procedure for the acetate salt.¹⁹ **5L** (0.2512 g, 0.51 mmol) was dissolved in 25 mL of methanol, and, separately, CuSO₄·5H₂O (0.3729 g, 1.50 mmol) was dissolved in 35 mL of methanol. The solution of **5L** was slowly added to the CuSO₄·5H₂O, resulting in a dark blue solution. The solution was stirred overnight, and the methanol was allowed to evaporate. **5** was collected as dark blue crystals in 63.9% yield (0.2372 g).

2.2. Refinement

A crystal was harvested under oil in ambient conditions and placed at the tip of a polyimide loop. The crystal was mounted in a stream of cold N₂ and centered in the X-ray beam using a video camera. Low-temperature (100 K) X-ray diffraction data comprising ϕ - and ω -scans were then collected using a MACH3 kappa goniometer coupled to a Bruker Apex II CCD detector with a Bruker-Nonius FR591 rotating anode X-ray source producing Cu K α radiation ($\lambda = 1.54178$ Å). The Bruker APEX3 suite was used to process the data; reflection intensities were integrated through the program SAINT, and appropriate absorption corrections were applied to the intensities via a multi-scan method using the program SADABS.

The structure was solved using dual-space methods in SHELXT²⁰ and refined against F^2 ²¹ on all data by full-matrix least squares with SHELXL-2014²¹ using established refinement strategies.²² All non-hydrogen atoms were refined anisotropically. The positions of all hydrogen atoms bound to carbon were calculated geometrically and refined using a riding model. The

positions of hydrogen atoms bound to the amine (N1-N8), alcohol (O1s), and fully occupied water (O3 and O4) groups were taken from the difference Fourier synthesis and subsequently refined semi-freely with the help of appropriate distance restraints. The isotropic displacement parameters of all hydrogen atoms were constrained to be 1.2 times the U_{eq} value (1.5 for methyl hydrogens) of the atom to which they are bound. For the final cycle of refinement, reflections obstructed by the beamstop or clear outliers were omitted.

3. Results and Discussion

3.1. Synthesis of **3L** and **3**

To make the novel compound containing cyclen and adamantyl (**3L**), 1-(bromomethyl)adamantane was added to cyclen, precipitated from the solution, and purified by rinsing with acetonitrile. Because **3L** was insoluble in polar solvents and copper sulfate was insoluble in non-polar solvents, aqueous copper sulfate was combined with solid **3L**. Complex formed, remained in the aqueous phase, and was recrystallized from methanol.

Complexes **3** and **3L** were characterized as discussed below. The characterization of all other ligands and complexes matched the characterization provided in their respective literature references. The characterizations of **1**, **2**, **4**, **4L**, **5**, and **5L** will not be discussed here.

^1H -NMR spectra were collected for **3L** (Figure 3.2) and with deuterated methanol added to determine the amine peak (Figure 3.3). Spectra were also collected for **3** without (Figure 3.4) and with (Figure 3.5) deuterium chloride (DCl) added to remove the copper's paramagnetic influence on the ligand. Thus, the **3L** spectrum should be equivalent to the spectrum for **3** plus DCl. However, unlike **1** and **2**, **3** was unchanged by trifluoroacetic acid, indicating that the Cu-N bonds were much stronger in **3**. Thus, the broad peaks seen in the spectrum of **3** plus DCl may indicate that, even with the stronger acid, the copper was only partially removed from the ligand.

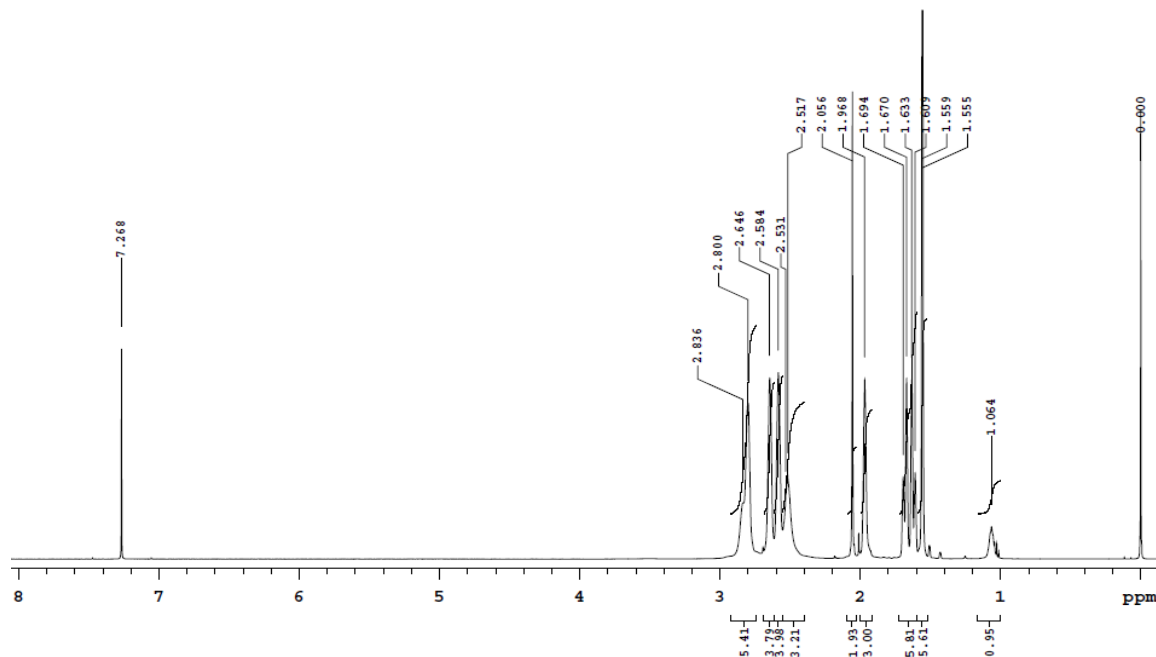


Figure 3.2: ^1H -NMR (500 MHz) of **3L** in CDCl_3 before addition of methanol- d_4 . Peak assignments (ppm): 7.27 (s, CHCl_3), 2.84 (s, 2H, NH), 2.80 (s, 4H, cyclen CH_2), 2.65 (s, 4H, cyclen CH_2), 2.58 (s, 4H, cyclen CH_2), 2.52 (s, 4H, cyclen CH_2), 2.06 (s, 2H, bridging CH_2), 1.97 (s, 3H, adamantane CH), 1.65 (m, 6H, adamantane CH_2), 1.56 (d, 6H, adamantane CH_2), 1.06 (s, 1H, NH), 0.00 (s, TMS).

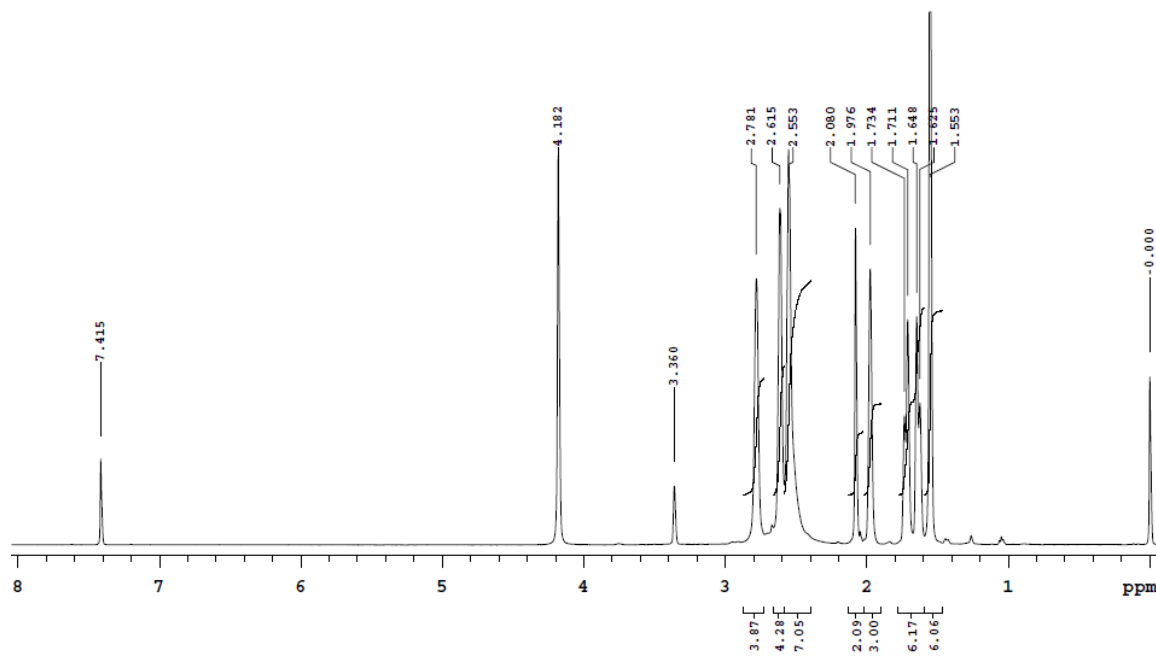


Figure 3.3: ^1H -NMR (500 MHz) of **3L** in CDCl_3 after addition of 2 drops of methanol- d_4 . Peak assignments (ppm): 7.42 (s, CHCl_3), 3.36 (CH_3OH), 2.78 (s, 4H, cyclen CH_2), 2.62 (s, 4H, cyclen CH_2), 2.55 (bs, 8H, cyclen CH_2), 2.08 (s, 2H, bridging CH_2), 1.98 (s, 3H, adamantane CH), 1.68 (m, 6H, adamantane CH_2), 1.55 (d, 6H, adamantane CH_2), 0.00 (s, TMS).

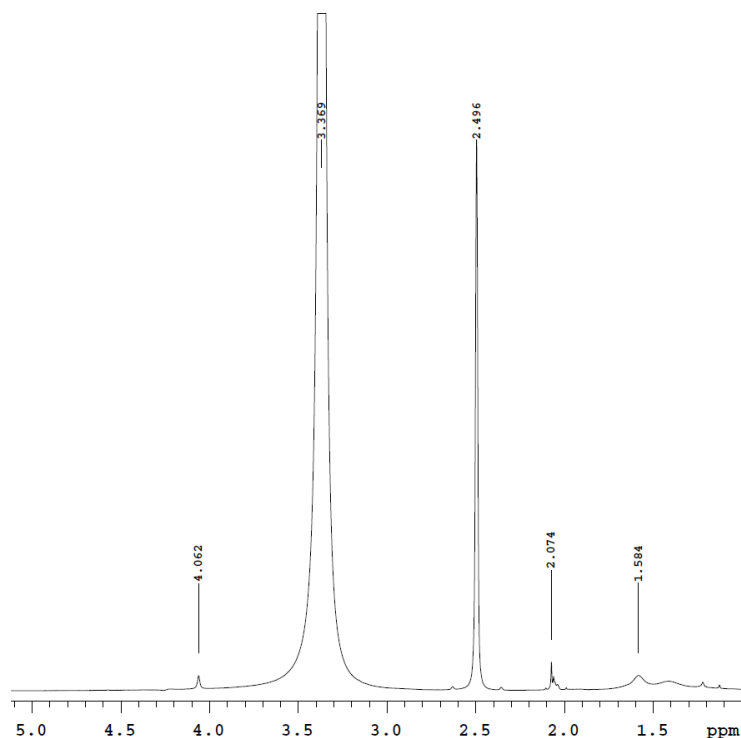


Figure 3.4: ^1H -NMR (500 MHz) of **3** in DMSO-d_6 before adding deuterium chloride. Peak assignments (ppm): 3.37 (s, H_2O), 2.50 (s, DMSO).

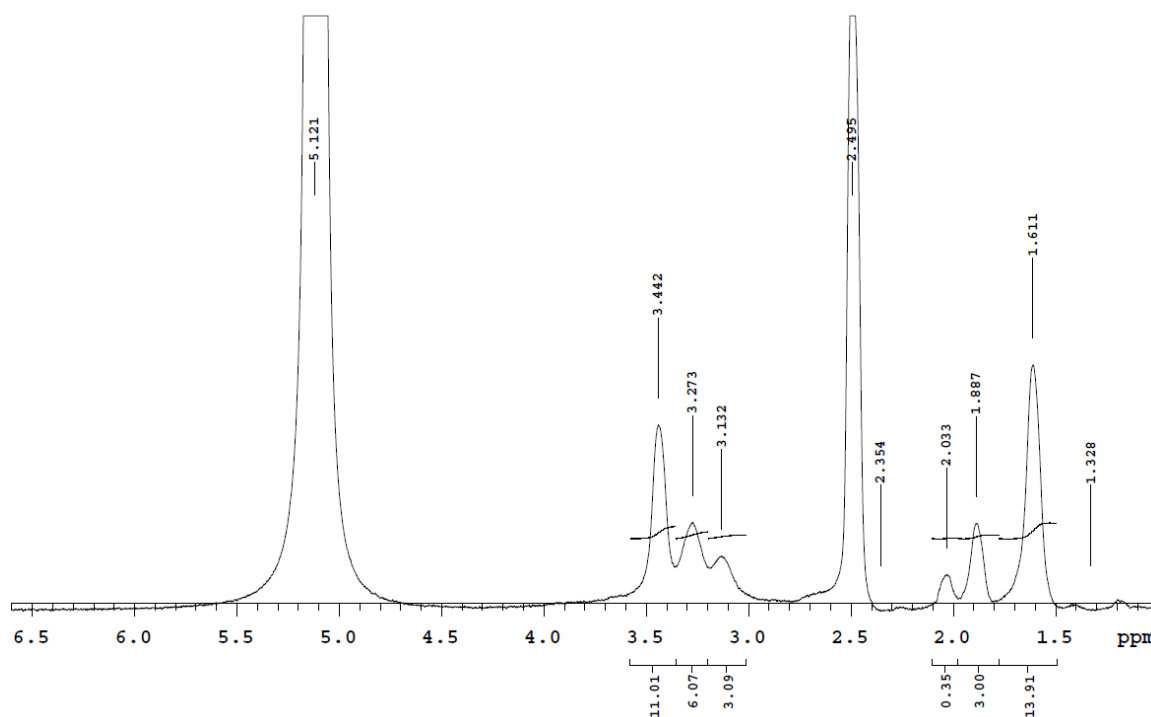


Figure 3.5: ^1H -NMR (500 MHz) of **3** in DMSO-d_6 after addition of deuterium chloride. Peak assignments (ppm): 5.12 (bs, H_2O), 3.44 (bs, 12H, cyclen non- α - CH_2), 3.27 (bs, 4H, cyclen α - CH_2), 3.13 (bs, 2H, bridging CH_2), 2.50 (s, DMSO), 2.03 (bs, 3H, adamantane CH), 1.89 (bs, 4H, adamantane CH_2 spatially closer to Cu), 1.61 (bs, 8H, adamantane CH_2).

This made integration somewhat unreliable, and it also resulted in unique splitting of the adamantyl CH₂ peaks, with those closer in proximity to the copper ion being split from the others (Fig. 3.10 for spatial referencing).

Mass spectra were obtained on a high-resolution mass spectrometer (HRMS) for **3** and **3L**. The spectrum for **3L** contained a standard M+H⁺ peak (321.3012 m/z) and was otherwise clean (Figure 3.6). The spectrum for **3** contained peaks for M-H⁺ (382.2151 m/z) and M+CHO₂⁻ (428.2210 m/z), with formate coming from the MS buffer (Figure 3.7). The MS instrument is set to detect plus one species and thus the M²⁺ species is not observed. The M+2 isotope peak shows the complex contains one Cu.

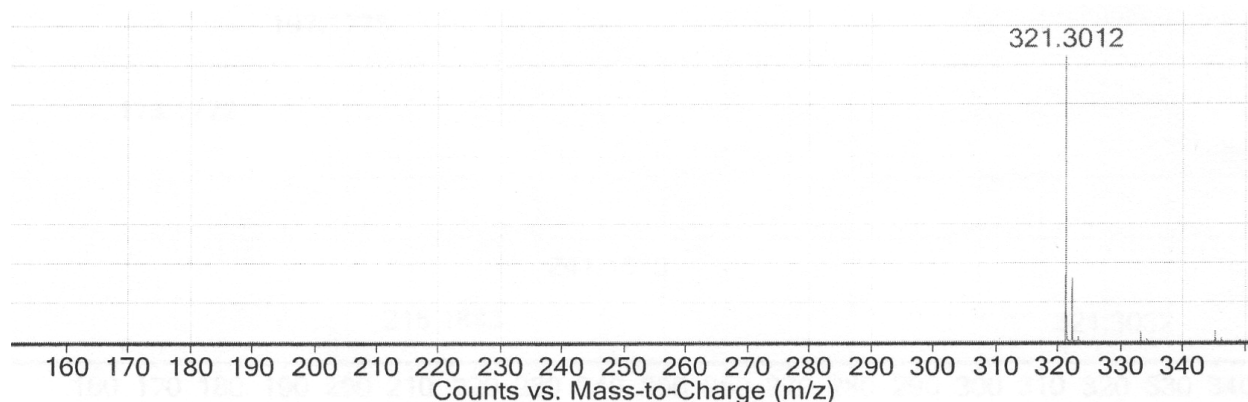


Figure 3.6. Mass spectrum of **3L**. The compound was found as an M+H peak at 321.3012 m/z.

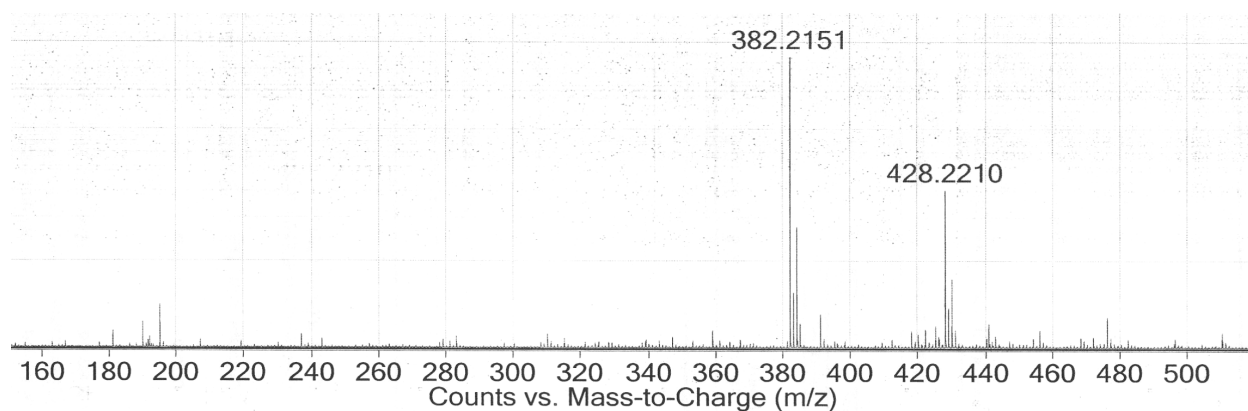


Figure 3.7. Mass spectrum of **3**. The complex was found as an M-H peak at 382.2151 and an M+CHO₂⁻ peak at 428.2210.

3.2. Crystal structures

Crystals of **1** (from blue solid of second crop) and **2** were grown from a concentrated solution in methanol, to which was slowly added diethyl ether in a 2:1 ratio of ether to methanol to form two layers, which were allowed to mix slowly. The first crystals of **1** were discarded for lack of clarity, and single crystals were grown from the mother liquor by slow evaporation followed by further addition of diethyl ether. Crystals of **3** were grown from methanol in the presence of acetone vapors in a sealed container. All crystals were left in their respective mother liquors until harvesting immediately before measurement by SC-XRD. Table 3.1 shows crystallographic data collected and parameters used. Included is data about the crystal itself, parameters of the data collection, and parameters for the pattern refinement.

Several anions were considered to counterbalance the copper charge for crystallization, as seen in complexes **1-3**. Both chloride (**1**) and perchlorate (**2**) were chosen for test syntheses because they were easy to use for synthesis, though recrystallizing **2** was markedly easier than recrystallizing **1**. This was thought to be due to the perchlorate, as a larger anion, being able to pack better, creating a tighter, more stable lattice with little room for disorder. Some intermolecular hydrogen bonds were also observed in **2**, but as perchlorate is a relatively weak hydrogen-bond acceptor, this probably had only a small effect on the overall formation and stability of the crystal. While hydrogen bonding existed in **1**, it was only from the free chloride, and that at only one point on each molecule, leaving most of the looser solid lattice more capable of disorder (Figure 3.8). While **2** seemed like the better choice, the dangers of perchlorate salts, both as physiological oxidizers and as dry solids, made it unusable as a potential drug candidate. Sulfate was chosen as a physiologically benign anion capable of multiple binding methods, such as stronger hydrogen bonds than those of perchlorate. The sulfate equivalent of **1** and **2** (not

shown) was synthesized as a proof of concept before copper sulfate was used in the synthesis of **3-5**.

Table 3.1. Crystallography data for **1**, **2**, and **3**. Data were collected on a Bruker Apex II CCD at 100K with Cu $K\alpha$ radiation. Absorption correction performed semi-empirically from equivalents.

Property	1	2	3
<i>Crystal data</i>			
Chemical formula	$\text{Cu}(\text{C}_8\text{H}_{20}\text{N}_4)(\text{ClO}_4)_2$	$\text{Cu}(\text{C}_8\text{H}_{20}\text{N}_4)\text{Cl}_2$	$\text{Cu}(\text{C}_{19}\text{H}_{36}\text{N}_4)(\text{H}_2\text{O})(\text{SO}_4)(\text{C}_2\text{H}_6\text{O})_{0.5}$
M_r	434.72	306.72	498.14
Crystal system, space group	Monoclinic, $P2_1/n$	Tetragonal, $P4_212$	Triclinic, P-1
a, b, c (Å)	8.8994 (4), 15.0259 (6), 11.8776(5)	9.3424 (10), 9.3424 (10), 7.3854 (8)	7.3851 (5), 16.6885 (12), 20.2197 (15)
α, β, γ (°)	90, 92.797 (2), 90	90, 90, 90	79.850 (3), 83.065 (3), 81.780 (3)
V (Å ³)	1586.40 (12)	644.60 (15)	2416.1 (3)
Z	4	2	2
μ (mm ⁻¹)	5.498	6.011	2.487
Crystal size (mm)	0.15 x 0.13 x 0.04	0.44 x 0.30 x 0.14	0.33 x 0.25 x 0.18
<i>Data collection</i>			
T_{\min}, T_{\max}	0.464, 0.585	0.134, 0.273	0.556, 0.661
No. of measured, independent and observed [$I > 2\sigma(I)$] reflections	19935, 2898	8661, 597	53713, 8764
R_{int}	0.0506	0.0451	0.0493
<i>Refinement</i>			
$R[F_2 > 2\sigma(F_2)], wR(F_2), S$	0.0275, 0.0754, 1.076	0.0232, 0.0574, 1.110	0.0320, 0.0849, 1.030
No. of reflections	19935	8661	8764
No. of parameters	220	125	677
No. of restraints	4	54	1366
$\Delta\rho_{\text{max}}, \Delta\rho_{\text{min}}$ (e Å ⁻³)	0.54, -0.35	0.34, -0.59	0.50, -0.46

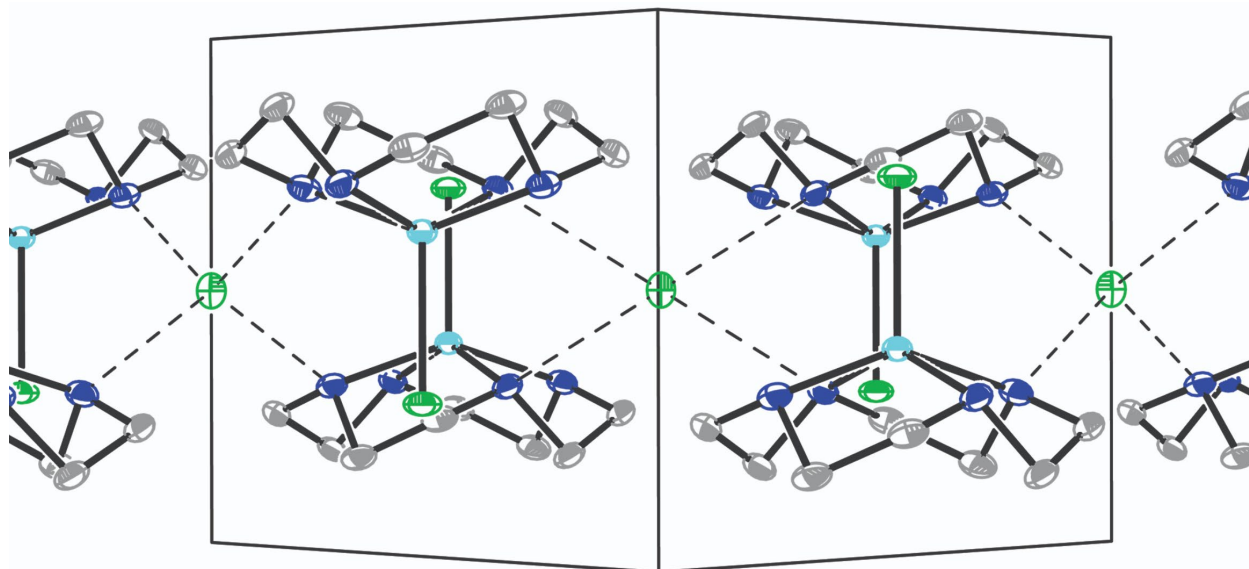


Figure 3.8. Hydrogen bonding in the crystal lattice of **1**. Gray spheres are carbon, dark blue are nitrogen, cyan are copper, and green are chlorine. Hydrogens have been left off, but reside on the nitrogens.

The three copper-cyclen complexes for which crystal structures were determined (**1-3**) were compared to a crystal structure of $[\text{CuH}_2\text{O}(\text{cyclen})]\text{SO}_4 \cdot 2\text{-}3\text{H}_2\text{O}$ (**6**) from the literature.¹³ All of the structures were similar in that they crystallized in a distorted square-pyramidal geometry with the metal center “puckered” above the plane of the four nitrogens (plane_N , Figure 3.9). Our group has seen a similar trait of copper to assume a distorted geometry between square pyramidal and trigonal bipyramidal in $\text{Cu}(\text{Amt-IDA})$ from our previous work. This tendency was attributed to Jahn-Teller distortion producing a decreased energy state with two of the metal-ligand bonds axial rather than only one,⁷ which was supported by the “puckering” effect decreasing in the order **1** > **3** > **6** > **2** as the structure was stabilized by increasing rigidity in the crystal lattice due to hydrogen bonding (Table 3.2).

Interestingly, **1** crystallized in an inverted-twin fashion, making it unique among the found $\text{Cu}(\text{cyclen})$ crystal structures. The twin structures were subjected to Mercury’s automatic overlay feature allowing free rotation, but the best overlay (not shown) looked much like the actual

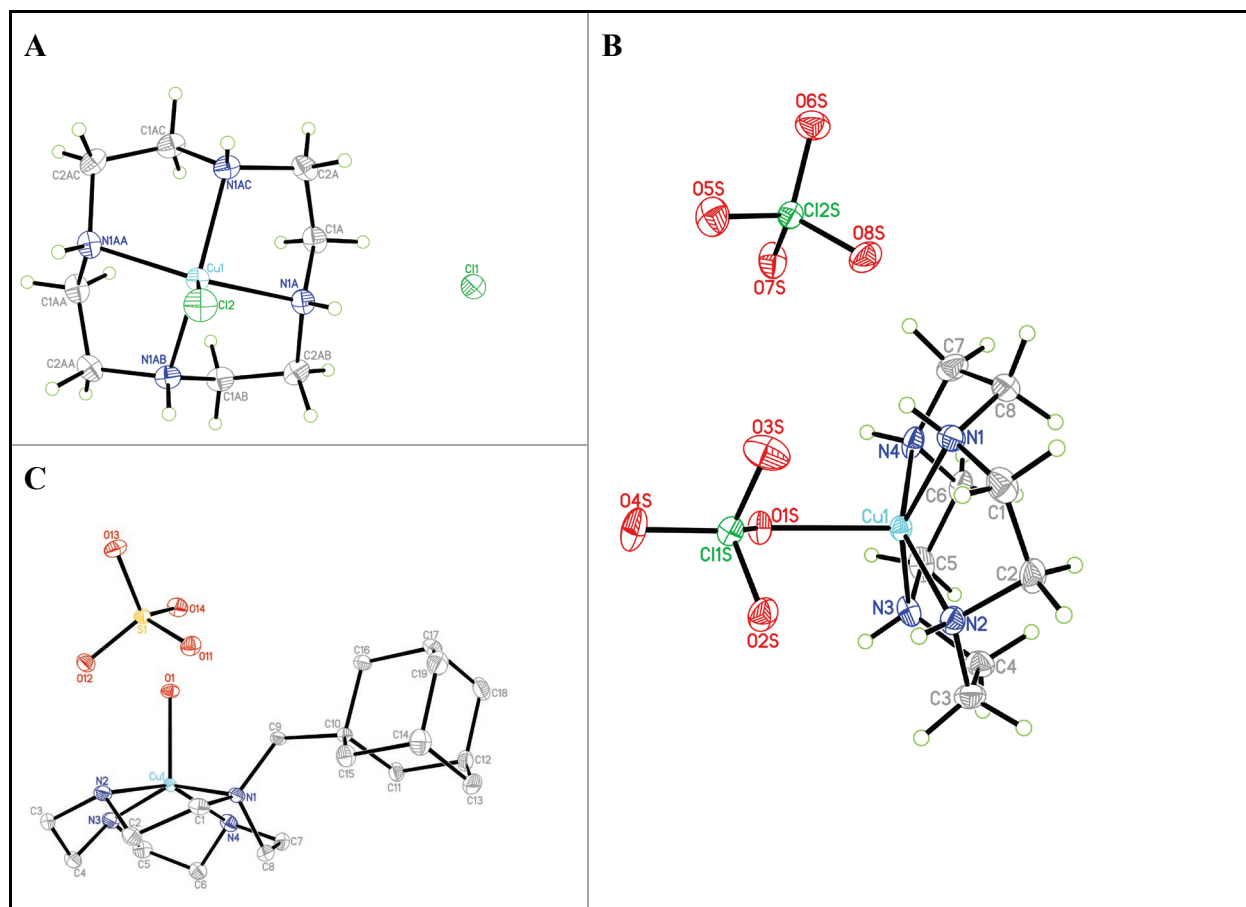


Figure 3.9. Crystal structures of (A) **1**, (B) **2**, and (C) **3**. Gray spheres are carbon, dark blue are nitrogen, cyan are copper, green are chlorine, red are oxygen, and yellow are sulfur.

Table 3.2. Selected bond lengths and distances (Å). Calculated values listed represent the average of multiple close values. Real values less than ± 0.005 Å from the average were used where available with their uncertainty included.

Length	1 ^a	2	3 ^b	6 ^c
Cu-plan _N dist. ^{c,d}	0.630	0.480	0.546	0.530
Cu-N length	1.995(8), 2.081(6)	2.0108(17)	2.0921(15), 2.0203(16)	2.116
Bisecting N-N dist. ^c	3.967	3.894	3.972, 3.885	3.902
N-C length	1.479(10), 1.473(12)	1.483(3)	1.493, 1.482(2)	1.482
C-C length	1.52(2), 1.49(3)	1.517(3)	1.518(3), 1.508(3)	1.517

^aSeparated values represent the two conformers **1A** and **1B**, respectively. ^bSeparated values represent the substituted nitrogen and unsubstituted nitrogens, respectively, or, for the C-C length, carbons adjacent to the same. ^cValues measured in Mercury software. ^dThe distance between the copper ion and the plane formed by the four nitrogens.

crystal structure (Figure 3.10). However, when inversion was allowed, the structures superimposed almost perfectly, though the small differences can be attributed to known refinement difficulties of inversion twins. Indeed, the two disordered parts of the cyclen moiety had opposite hands; the nitrogen atoms in the major component (N1A, 53% occupancy) exhibited S chirality, and the nitrogen atoms in the minor component (N1B, 47% occupancy) exhibited R chirality, though they were nearly equally represented. This disorder combined with the somewhat ambiguous absolute structure of inversion twins indicated that both hands were equally likely. In addition to coordinating with the copper center, the disordered amine groups may have had some hydrogen bond-like interaction with the free-standing chloride counterion. Each noncoordinating chloride ion has such interactions with four copper complexes, that the chloride has roughly tetrahedral geometry. This results in a quilt-like packing of the complexes in layers parallel to the *ab* plane with the thickness of each layer being the width of the *c*-axis.

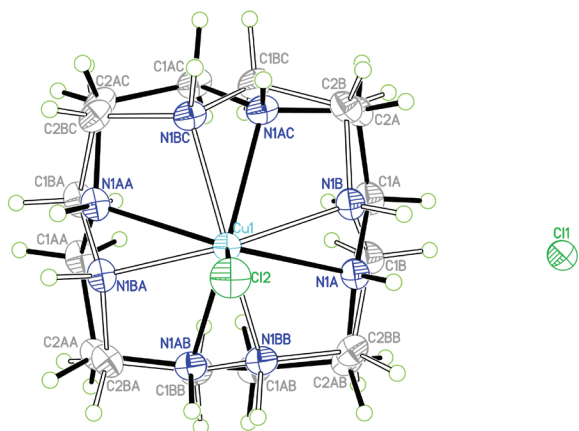


Figure 3.10. Crystal structures of two conformers of **1**. The copper and two chlorides were aligned as static reference points. **1A** is shown with black lines and **1B** is shown with white lines, with individual atoms labeled as A or B, respectively. Gray spheres are carbon, dark blue are nitrogen, cyan is copper, and green are chlorine.

The closest analogue of **3** was **6**, with which it had both several commonalities and several differences. In both, the copper bonded with a solvent molecule, allowing the free sulfate, along with other solvents of crystallization, to form a strongly interlaced hydrogen-bonding lattice.

This can be seen on the hydrophilic end of **3** (Figure 3.11). Both were different than **1** and **2** in that the copper center was bound to a solvent molecule instead of a counterion, and both **3** (0.546 Å) and **6** (0.530 Å) had roughly the same Cu-plane_N distance relative to the distances seen in **1A** (0.630 Å) and **2** (0.480 Å). The N-C length of **6** (1.482 Å) matched the N-C length on the unsubstituted nitrogen of **3** (1.482 Å) and was close to that for **1A** and **2** (1.479 Å and 1.483 Å, respectively) while the C-C length of **6** (1.517 Å) closely matched the C-C length of **3** (1.518 Å) for the carbons adjacent to the substituted nitrogen and that of **2** (1.517 Å).

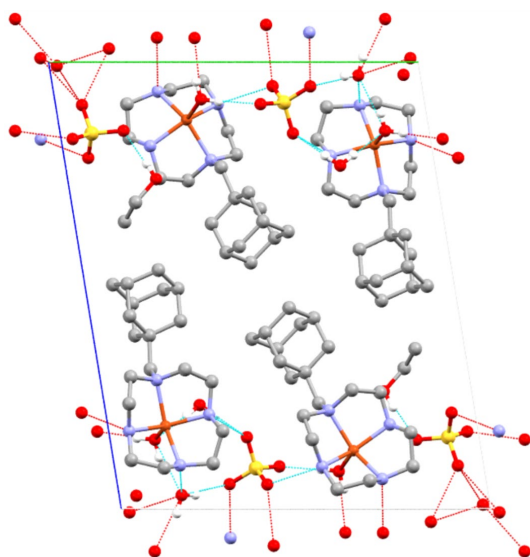


Figure 3.11. Hydrogen bonding in the crystal lattice of **3**. Two unit cells are shown. Cyan lines are hydrogen bonds within the unit cells shown, and red lines are hydrogen bonds extending to other unit cells. Gray spheres are carbon, dark blue are nitrogen, orange are copper, yellow are sulfur, and red are oxygen.

Of interest for **3** is that the N-Cu-N distance extending straight across from the substituted nitrogen is the longest of all the N-Cu-N distances (3.972 Å), while the N-Cu-N distance extending between the non-substituted nitrogens is the shortest of all of them (3.885 Å). These values are slightly different from **1**, the least rigid structure, for the longest (3.967 Å) and **2**, the most rigid structure, for shortest (3.894 Å). This suggests that the amantadine, which can freely rotate at two points and relies on hydrophobic interactions for packing, decreases the rigidity of

the structure along the connecting axis, while the other axis maintained stability with increased rigidity along the axis that promoted the far better hydrogen-bonding lattice (Figure 3.12).

The packing arrangement of **3** lies with the hydrophobic adamantane cages facing toward each other. The hydrophilic rings, counterions, and solvent molecules face toward each other in an ABAB pattern of complexes extending along the *b*-axis. Together, the alternating hydrophilic and hydrophobic *b*-axis “threads” form sheets along the *ab* plane.

The short, stable N-Cu-N axis of **3** followed the hydrophilic threads of the sheet, which contain numerous hydrogen-bonding opportunities, while the hydrophobic amantadyl threads were left to rely mostly on hydrophobic interactions for stability. Uniquely, though, the unit cell of **3** contained two full

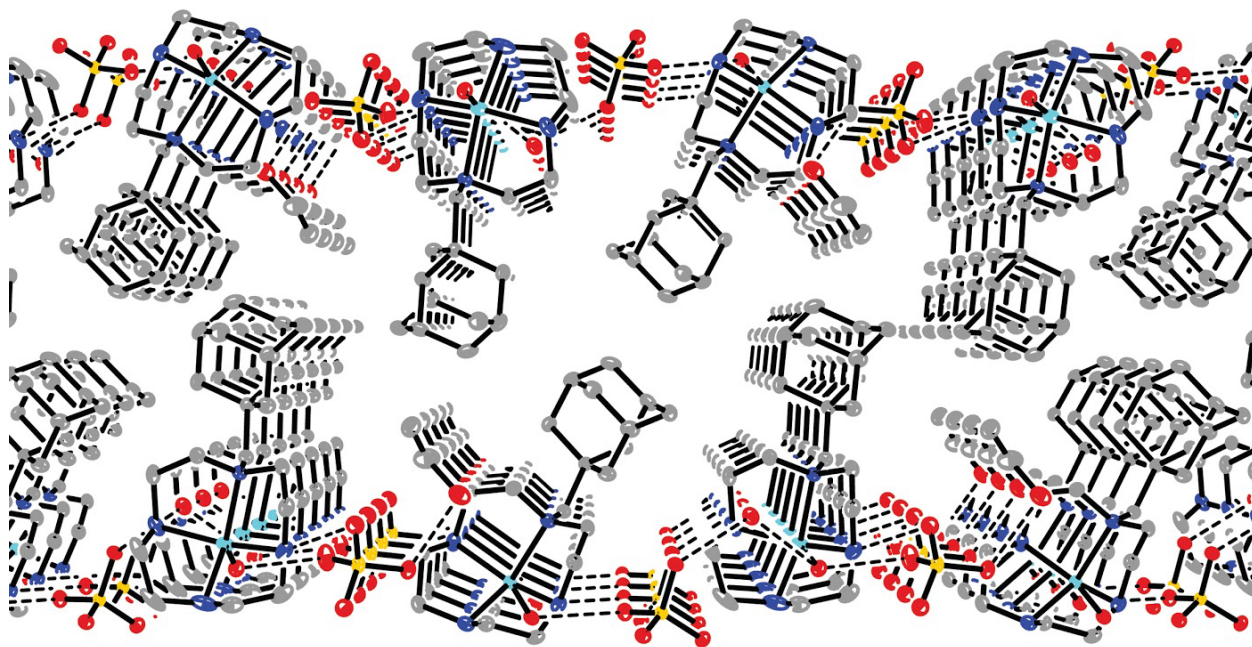


Figure 3.12. Crystal packing structure of **3**. Gray spheres are carbon, dark blue are nitrogen, cyan are copper, yellow are sulfur, and red are oxygen.

molecules placed side by side yet slightly askew from each other, and each of the two molecules’ counterions crystallized in a different orientation, presumably to allow for a more stable crystal lattice. Contrarily, in the packing arrangement of **2**, in which every molecule was identical, two

molecules of compound lay tightly packed with their bound perchlorate counterions pointing inward toward the ring of the other molecule in a shoe-like orientation, and the ring pointed out. These units then packed sideways on top of each other, forming dense, independent columns extending along the *c*-axis. In contrast to the packing structure for **3** and **1** (Figure 3.13), in which the cyclen rings are parallel with the *ab* plane, the packing structure of **2** formed with the cyclen rings lying parallel to the *bc* plane (Figure 3.14).

3.3 Viral studies

Aqueous solutions of complexes **1-5** were introduced to M2A, and *in vitro* TEVC assays and efficacy studies were performed for the complexes as explained in our previous work.⁷ The previous complexes exhibited superior performance to all complexes in this study in the inhibition of M2A and IVA-M2A. This could have been due to size constraints of the complexes in this study, as the complexes were significantly larger than our previous work. Due to the copper's ability to only bind through an axial site in the cyclic complexes, the Cu-His binding may not have been strong enough to overcome displacement by ambient hydroniums at acidic pH levels. The possible exception to this was **5**, in which the fourth equatorial site was freer than the cyclic complexes, though the steric crowding from the bis-pyridyl rings still made that equatorial site less available to the imidazole nitrogen than Cu(Amt-IDA),^{19,7} especially if the sterics were exacerbated by any repulsion between the aromatic π -electron clouds. Additionally, because M2A is gated with a nonpolar V27 cluster, it may have rejected the highly polar divalent complexes simply due to electrostatic incompatibility. Positive ions inside M2A, which is known to house hydronium and sodium ions, may have prevented the complexes from entering to a useful degree due to electromagnetic repulsion. Finally, because at least three of the H37 histidines are protonated when the channel is active, the repulsive positive charge of the H37

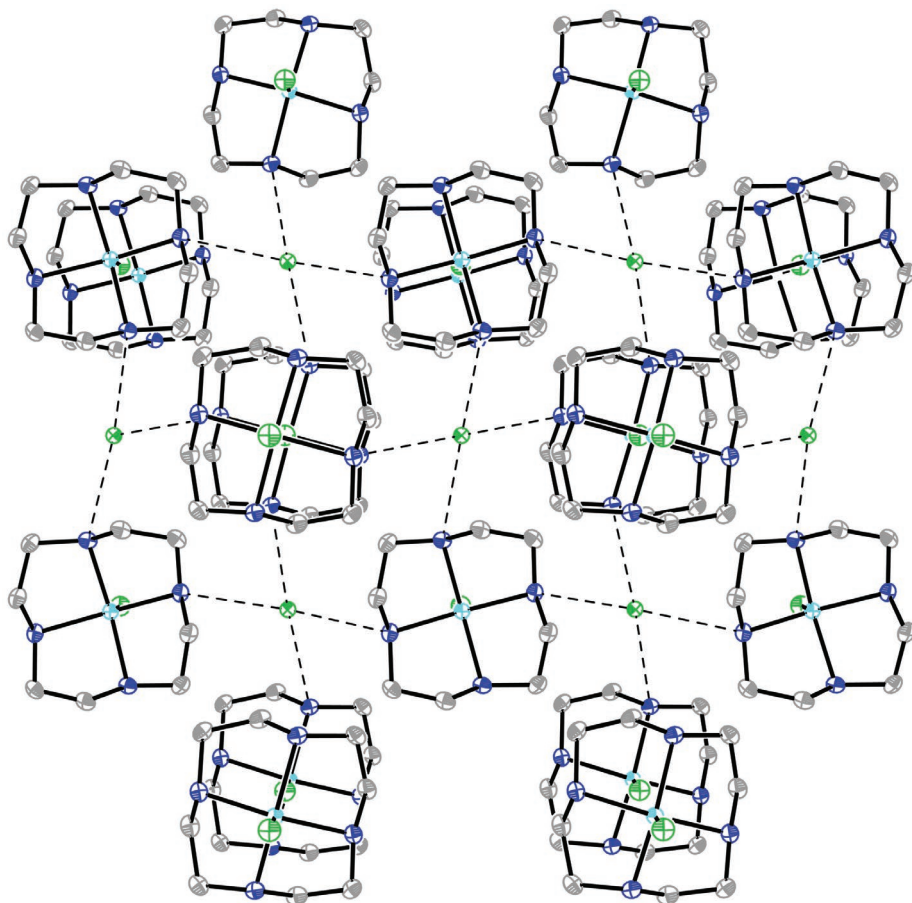


Figure 3.13. Crystal packing structure of **1**. Gray spheres are carbon, dark blue are nitrogen, cyan are copper, and green are chlorine.

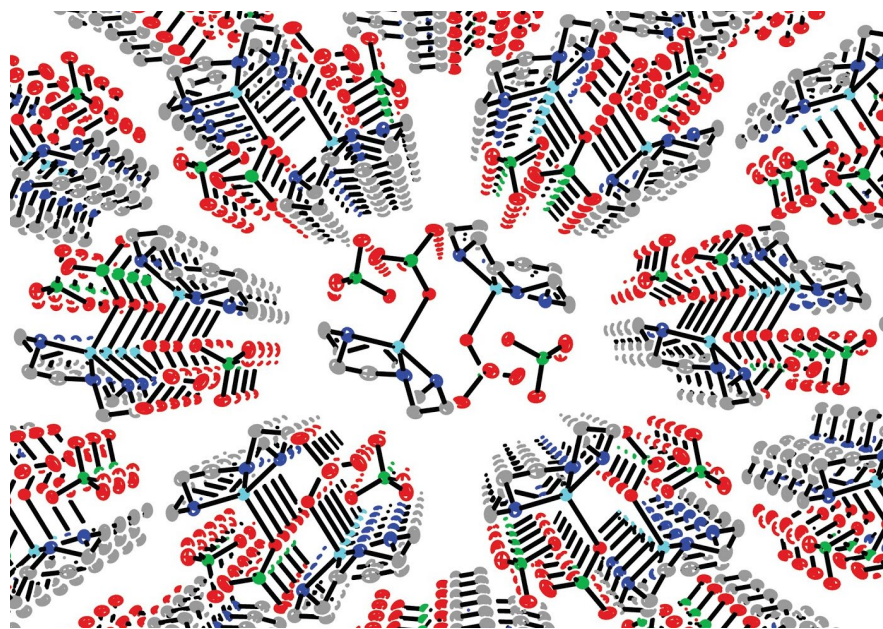


Figure 3.14. Crystal packing structure of **2**. Gray spheres are carbon, dark blue are nitrogen, cyan are copper, green are chlorine, and red are oxygen.

cluster—believed to be strong enough to drive the conformation change of the channel—may have repelled the unmitigated, divalent charge of the copper ion, preventing it from binding to the histidines.

4. Conclusions

A series of divalently charged copper complexes were synthesized containing three or four aza or amino nitrogens. The ligand of one of these, **3L**, was new, as was its sulfated copper complex, **3**, and the crystal structure thereof. Procedures for the novel syntheses of **3L** and **3** were created, and the crystal structure of **3** was solved. In addition, the crystal structures of **1** and **2** were unknown to the CCDC database, so those structures were also solved from single crystals. Of interest for **1** was the inverted twin crystallization structure, each of which displayed opposite chirality in equal proportion. In **2**, the much tighter packing structure formed independent columns consisting of stacked, interposed pairs of molecules, though the independent columns were packed loosely from one another. **3** displayed an interesting arrangement of sheets formed with alternating “threads,” one with hydrophobic adamantanes pointing toward each other and the other with the hydrophilic rings and ions pointing toward each other. This left the cyclen axis with the adamantyl substitution relatively weak with longer bonds and N-Cu-N distances than those of the other axis, which lay along the hydrophobic threads and was made stronger by interlaced hydrogen bonding.

Complexes **1-5** were tested against M2A-S31N, and they exhibited neither significant channel inhibition nor efficacy in saving infected MDCK cells compared to previous work. This could be explainable by the size, electrostatic makeup, and/or binding options of the complexes preventing them from binding the M2A-H37 residues at acidic pH. However, though divalently-charged complexes were shown relatively ineffective, monovalently-charged complexes may

fare better, as the channel is designed to accommodate singly-charged ions. These complexes could be a hybrid of our work performed here and that performed previously, binding the copper ion with one anionic arm and one neutral arm joined by an Amt or CO scaffold.

Acknowledgements

Ethan Damron, Daniel Johnston, and Mikki Twiggs provided assistance in design and synthesis. Biological testing was performed by students in Dr. David Busath's group in the BYU Department of Physiology and Developmental Biology. The work was supported by a grant from National Institutes of Health (AI 23007), a BYU College High Impact Research Proposal award, and BYU Mentoring Environment Grants. The funding sources had no involvement in design, execution, or communication of the report.

References

1. Cheng, P. Y.; Palekar, R.; Azziz-Baumgartner, E.; Iuliano, D.; Alencar, A. P.; Bresee, J.; Oliva, O.; de Souza, MDM; Widdowson, M. A. (2015). *Influenza Other Respir. Viruses* **9**, Suppl 1:13-21.
2. Bright, R. A.; Shay, D.; Bresee, J.; Klimov, A.; Cox, N; Ortiz, J. (2006). *Morb. Mortal. Wkly. Rep.* **55**, 44-46.
3. Wang, C.; Takeuchi, K.; Pinto, L. H.; Lamb, R. A. (1993). *J. Virol.* **67**, 5585-5594.
4. Gandhi, C. S.; Shuck, K.; Lear, J. D.; Dieckmann, G. R.; DeGrado, W. F.; Lamb, R. A.; Pinto, L. H. (1999). *J. Biol. Chem.* **274**, 5474-5482.
5. Su, Y.; Hu, F.; Hong, M. (2012). *J. Am. Chem. Soc.* **134**, 8693-8702.
6. Zhang, C. X.; Lippard, S. J. (2003). *Curr. Opin. Chem. Biol.* **7**, 481-489.
7. Gordon, N. A.; McGuire, Kelly L.; Wallentine, S. K.; Mohl, G. A.; Lynch, J. D.; Harrison, R. G.; Busath, D. D. (2017). *Antiviral Res.* **147**, 100-106.
8. Bianchi, A.; Micheloni, M.; Paoletti, P. (1991). *Coordin. Chem. Rev.* **110**, 17-113.
9. Kim, S.; Jung, I.; Lee, E.; Kim, J.; Sakamoto, S.; Yamaguchi, K.; Kim, K. (2001). *Angew. Chem. Int. Ed.* **40**, 2119-2121.
10. Wang, J.; Lamb, J. D.; Hansen, L. D.; Harrison, R. G. (2010). *J. Incl. Phenom. Macrocycl. Chem.* **67**, 55-61.
11. Wang, J.; Lamb, J. D.; Hansen, L. D.; Harrison, R. G. (2009). *J. Chromatogr. Sci.* **47**, 510-515.
12. Tsebrikova, G. S.; Polyakova, I. N.; Solov'ev, V. P.; Ivanova, I. S.; Kalashnikova, I. P.; Kodina, G. E.; Baulin, V. E.; Tsivadze, A. Y. (2018). *Inorg. Chim. Acta* **478**, 250-259.

13. Pérez-Toro, I.; Domínguez-Martín, A.; Choquesillo-Lazarte, D.; Vélchez-Rodríguez, E.; González-Pérez, J. M.; Castiñeiras, A.; Niclós-Gutiérrez, J. (2015). *J. Inorg. Biochem.* **148**, 84-92.
14. Clay, R.; Murray-Rust, P.; Murray-Rust, J. (1979). *Acta Cryst.* **B35**, 1894-1895.
15. Štimac, A.; Šekutor, M.; Mlinarić-Majerski, K.; Frkanec, L.; Frkanec, R. (2017) *Molecules* **22**, 297-310.
16. Kruppa, M.; Frank, D.; Leffler-Schuster, H.; König, B. (2006). *Inorg. Chim. Acta* **359**, 1159-1168.
17. Courant, T.; Roullin, V. G.; Cadiou, C.; Delavoie, F.; Molinari, M.; Andry, M. C.; Chuburu, F. (2009). *Int. J. Pharm.* **379**, 226-234.
18. Wu, Q.; Lee, M. L.; Harrison, R. G. (2002). *J. Chromatogr. A* **954**, 247-258.
19. Zhou, Y.; Tao, J.; Lv, Q.; Jia, W.; Yun, R.; Cheng, Y. (2015). *Inorganica Chim. Acta* **426**, 211-220.
20. Sheldrick, G. M. (2015). *Acta Cryst.* **A71**, 3–8.
21. Sheldrick, G. M. (2015). *Acta Cryst.* **C71**, 3–8.
22. Müller, P. (2009). *Crystallography Reviews* **15**, 57-83.